

OPECAL

D12:ATBD RADIOMETRY MONITORING USING DESERT SITE

TECHNICAL NOTE

	Name	Company	Date	Signature
Prepared by :	B. Berthelot	Magellium	02/11/2014	
Checked by :		Magellium		
Approved by :	B. Berthelot	Magellium	02/11/2014	

Document reference :	OPECAL-TN-043-MAG
Issue.Revision :	1.1
Date :	16/12/2014
Client :	ESRIN
Ref., Tender :	AO/1-7043/11/F/MOS

Distribution list

	Name	Company	N. copies
Addresses :	M. Bouvet G. Ottavianelli	ESA/ESTEC ESA/ESRIN	1
Internal copy :	Customer file Project Manager Development team	Magellium Magellium Magellium	1 (digital) 1 (digital) 1 (digital)

Document Change Record

Iss.	Rev.	Date	Reason	Comments
1	0	02/11/2014	Creation of the document	
1	1	03/12/2014	Answers to ESA comments	

Table of contents

1 Objectives of the document	8
1.1 Related documents	8
1.1.1 Applicable documents	8
1.1.2 Reference documents	8
1.1.3 Bibliography	9
1.1.4 Acronyms	9
2 Introduction	11
3 Algorithm overview	12
3.1 Principle of the method	12
3.1.1 Method	13
3.1.1.1 Stability monitoring	13
3.1.1.2 Multitemporal monitoring	13
3.1.2 Modelling	14
3.1.2.1 SMAC	14
3.1.2.2 BRDF	14
3.1.2.2.1 KERNEL description	14
3.1.2.2.2 MCD43B1 product description	15
3.1.2.3 Atmosphere characteristics	16
3.2 Implementation description	17
3.2.1 Overall steps	17
3.2.2 Detailed steps	17
3.2.2.1 Input data selection	17
3.2.2.2 Auxiliary data extraction	18
3.2.2.3 Pixel selection	18
3.2.2.4 Correct TOA reflectances from gaseous transmission	18
3.2.2.5 RTM Solar Irradiance correction	18
3.2.2.6 Read BRDF model coefficient interpolated at the date of the acquisition in the 7 MODIS bands	20
3.2.2.7 Simulate the BRDF in the 7 MODIS bands for the geometry of the sensor	20
3.2.2.8 Spectral interpolation	20
3.2.2.9 TOA reflectance estimation	21
3.2.2.10 $\Delta\rho$ estimation in the all band	21
3.2.2.11 Statistical analysis of the sensor radiometry	21
3.2.3 Auxiliary data	21
3.2.3.1 Thresholds	21
3.2.3.2 Filtered BRDF	21
3.2.4 Ancillary data	23
4 Dataset analysis to monitor the sensor radiometry using desert site	24
4.1 Analysis of MODIS	24
4.1.1 Details of results for a single date	24
4.1.2 Multiyear results	30
4.2 Analysis of MERIS	33
4.2.1 Details of results for a single date	33

4.2.2	Multiyear results	39
4.3	Analysis of PARASOL.....	42
4.3.1	Details of results for a single date	42
4.3.2	Multiyear results	47
4.4	Analysis of AASTR	49
4.4.1	Details of results for a single date	49
4.4.2	Multiyear results	53
4.4.2.1	Results related to nadir view.....	53
4.4.2.1	Results related to forward view	54
4.5	Analysis of VEGETATION	56
4.5.1	Details of results for a single date	56
4.5.2	Multiyear results	60
5	Error Analysis	62

List of the Tables

Table 1: List of applicable documents.....	8
Table 2: List of reference documents	8
Table 3: MODIS spectral band order	15
Table 4: Solar irradiance	19
Table 4: Threshold used to select data	21
Table 5: Ancillary data needed in the DESERT method	23
Table 6: MODIS band name	26

List of the Figures

Figure 1: Libya 4 site seen by ETM (ETM+ Bands 321), source USGS.	12
Figure 2: K1 coefficient- Synthesis of June, Julian day 180, 2011	16
Figure 3: K2 coefficient- Synthesis of June, Julian day 180, 2011	16
Figure 4: K3 coefficient- Synthesis of June, Julian day 180, 2011	16
Figure 5: Variability of the K1 coefficient for three successive syntheses	22
Figure 6: Temporal profile of K0, K1, K2 for the five years. The green line is the filtered profile.	22
Figure 7: MODIS acquisition 04/01/2009 (Product MYD021KM.A2009004.1155.005.2009330144122.gscs_000500567696_hdf)	24
Figure 8: TOA reflectances in channels 1 and 2	25
Figure 10: Cloud mask	25
Figure 11: Scatterplot of simulated TOA reflectances versus measured TOA reflectances for all MODIS bands. Central wavelength in μm is indicated in a frame inserted in the figure.	27
Figure 12: TOA reflectance in the NIR. Measured (top left), Simulated (top right), difference estimated minus measured (bottom).....	28
Figure 13: Map of the reflectance ratio in the NIR band	28
Figure 14: Ratio of Measured to Simulated TOA reflectance histograms. Central wavelength in μm is indicated in a frame inserted in the figure.	29
Figure 15: Temporal variability of the mean ratio between 2008 and 2011	30
Figure 16: Temporal variability of the TOA reflectance (measured and simulated)	31
Figure 16: Temporal variability of the mean ratio of Measured to Simulated TOA reflectance versus Solar zenith Angle.....	32
Figure 18: MERIS acquisition 31/07/2010 (Product MER_RR__1PRBCM20100731_085850_000000562091_00365_44006_0001_N1)	33
Figure 19: Polar diagram showing the geometry of the acquisition. Solar and satellite configuration angles are represented in blue and red respectively.	33
Figure 20: TOA reflectances in channels 6 (left) and 13 (right).....	34
Figure 22: Cloud mask (left). Dilated cloud mask (right image)	34
Figure 23: Scatterplot of simulated TOA reflectances versus measured TOA reflectances for 13 MERIS bands. Bands 11 and 15 are not simulated.	36
Figure 24: TOA reflectance in the NIR. Measured (top left), Simulated (top right), difference estimated minus measured (bottom).....	37
Figure 25: Map of reflectance ratio in the NIR band	37
Figure 26: Ratio of Measured to Simulated TOA reflectance histograms.....	38
Figure 27: Temporal variability of the mean ratio between 2008 and 2011	40
Figure 26: Temporal variability of the TOA reflectance (measured and simulated)	41
Figure 27: Temporal variability of the mean ratio of Measured to Simulated TOA reflectance versus Solar zenith Angle.....	41
Figure 18: PARASOL acquisition 04/08/2009 (Product P3L1TBG1107109KD_n30_00_N26_00_e021_00_E027_00).....	42
Figure 19: Polar diagram showing the geometry of the acquisition. Solar and satellite configuration angles are represented in blue and red respectively.	42
Figure 20: TOA reflectances in channel 7 (right).....	43

Figure 23: Scatterplot of simulated TOA reflectances versus measured TOA reflectances for 6 PARASOL bands. Bands 5, 6 and 8 are simulated.....	44
Figure 24: TOA reflectance in the NIR. Measured (top left), Simulated (top right), difference estimated minus measured (bottom).....	45
Figure 25: Map of reflectance ratio in the NIR band	45
Figure 26: Ratio of Measured to Simulated TOA reflectance histograms.....	46
Figure 27: Temporal variability of the mean ratio between 2008 and 2011	47
Figure 26: Temporal variability of the TOA reflectance (measured and simulated)	48
Figure 27: Temporal variability of the mean ratio of Measured to Simulated TOA reflectance versus Solar zenith Angle.....	48
Figure 30: AATSR acquisition 15/06/2008 (ATS_TOA_1PNMAP20080615_084739_000000482069_00279_32898_0001_N1)	49
Figure 31: Polar diagram showing the geometry of the acquisition. Solar in blue, satellite in red.....	49
Figure 32: TOA reflectances in B0, B2, B3 SWIR channels	49
Figure 34: Cloud mask (left). Dilated cloud mask (right image)	50
Figure 35: Scatterplot of simulated TOA reflectances versus measured TOA reflectances for all AATSR bands	51
Figure 36: TOA reflectance in the NIR. Measured (top left), Simulated (top right), difference estimated minus measured (bottom).....	52
Figure 38: Map of reflectance ratio in the NIR band	52
Figure 37: Ratio of Measured to Simulated TOA reflectance histograms.....	53
Figure 39: Temporal variability of the mean ratio between 2008 and 2011	53
Figure 40: Temporal variability of the TOA reflectance (measured and simulated)	54
Figure 27: Temporal variability of the mean ratio of Measured to Simulated TOA reflectance versus Solar zenith Angle.....	54
Figure 39: Temporal variability of the mean ratio between 2008 and 2011	54
Figure 40: Temporal variability of the TOA reflectance (measured and simulated)	55
Figure 30: VEGETATION acquisition 31/07/2010 (V2KRNP____20080712F026).....	56
Figure 31: Polar diagram showing the geometry of the acquisition. Solar in blue, satellite in red.....	56
Figure 32: TOA reflectances in B0, B2, B3 SWIR channels	57
Figure 34: Cloud mask (left). Dilated cloud mask (right image)	57
Figure 35: Scatterplot of simulated TOA reflectances versus measured TOA reflectances for all VEGETATION bands	58
Figure 36: TOA reflectance in the NIR. Measured (top left), Simulated (top right), difference estimated minus measured (bottom).....	59
Figure 38: Map of reflectance ratio in the NIR band	59
Figure 37: Ratio of Measured to Simulated TOA reflectance histograms.....	60
Figure 39: Temporal variability of the mean ratio between 2008 and 2011	60
Figure 40: Temporal variability of the TOA reflectance (measured and simulated)	61
Figure 27: Temporal variability of the mean ratio of Measured to Simulated TOA reflectance versus Solar zenith Angle.....	61

1 Objectives of the document

The purpose of this study is to develop and implement a method to monitor sensor radiometry of optical sensors using desert site into DIMITRI software.

1.1 Related documents

1.1.1 Applicable documents

Table 1: List of applicable documents

Id.	Ref.	Description
AD1	QA4EO-QAEO-GEN-DQK-001/7, Version 4.0	QA4EO Guidelines (seven documents) http://qa4eo.org/

1.1.2 Reference documents

Table 2: List of reference documents

Id.	Ref.
RD 1.	Bouvet M. , Ramoino F., Radiometric intercomparison of AATSR, MERIS, and Aqua MODIS over Dome Concordia (Antarctica), Can. J. Remote Sensing, Vol. 36, No. 5, pp. 464–473, 2010. http://pubs.casi.ca/loi/cjrs
RD 2.	DIMITRI Software User Manual ftp://ftp.estec.esa.int/pub/gsp/anonymous/Earth_Observation_Multi-mission_Phase-E2_Operational_Calibration/DIMITRI_SUM.pdf
RD 3.	DIMITRI Software Design Document ftp://ftp.estec.esa.int/pub/gsp/anonymous/Earth_Observation_Multi-mission_Phase-E2_Operational_Calibration/DIMITRI_SDD.pdf
RD 4.	Statement of Word GSP activity ‘Towards the Intercalibration of EO Medium Resolution Multi-Spectral Imagers’ ftp://ftp.estec.esa.int/pub/gsp/anonymous/Earth_Observation_Multi-mission_Phase-E2_Operational_Calibration/SoW_GSP_TowardsTheIntercalibrationOfEOMediumResolutionMultiSpectralImagers.pdf
RD 5.	Hagolle et Al., Results of POLDER in-flight Calibration, IEEE Transactions on Geoscience and Remote Sensing, May 1999, Volume 37, Number 03 [p. 1550]. http://ieeexplore.ieee.org/xpl/RecentIssue.jsp?punumber=36
RD 6.	Vermote, E., R. Santer, P.Y. Deschamps and M. Herman, In-flight Calibration of Large Field-of-View Sensors at Short Wavelengths using Rayleigh Scattering, Int. Journal of Remote Sensing, 13, No 18, 1992. http://www.tandf.co.uk/journals/tres

RD 7.	Smith D., Poulsen C., Latter B.: Calibration Status of the AATSR Reflectance Channels, MERIS AATSR workshop 2008 proceedings. http://earth.esa.int/meris_aatsr_2008/
-------	--

1.1.3 Bibliography

- Ackerman, S. A., K. I. Strabala, W. P. Menzel, R. A. Frey, C. C. Moeller, and L. E. Gumley, 1998: Discriminating clear-sky from clouds with MODIS. *J. Geophys. Res.*, 103 (D24), 32 141-32 157.
- Berthelot, B.; Dedieu, G., "Operational method to correct VEGETATION satellite measurements from atmospheric effects," *Geoscience and Remote Sensing Symposium, 2000. Proceedings. IGARSS 2000. IEEE 2000 International*, vol.2, no., pp.831,833 vol.2, 2000
- Holben, B. N., Kaufman, Y. J., and Kendall, J. D., 1990, NOAA-11 AVHRR visible and near-IR inflight calibration: The International Journal of Remote Sensing, 11, 1511-1519.
- Kaufman Y.J., and B. N. Holben (1993). Calibration of the AVHRR visible and Near-IR bands by atmospheric scattering, ocean glint and desert reflection *Int. J. Rem. Sens.*, 14, 21-52 Cosnefroy et al., 1996,
- Kotchenova S.Y. & E.F. Vermote, Validation of a vector version of the 6S radiative transfer code for atmospheric correction of satellite data. Part II: Homogeneous Lambertian and anisotropic surfaces, *Applied Optics*, 2007.
- Kotchenova, S.Y., E.F. Vermote, R. Matarrese, & F.J. Klemm, Jr., Validation of a vector version of the 6S radiative transfer code for atmospheric correction of satellite data. Part I: Path Radiance, *Applied Optics*, 45(26), 6726-6774, 2006.
- Li, X. and Strahler, A.H. 1992. Geometric-optical bidirectional reflectance modeling of the discrete crown vegetation canopy: Effect of crown shape and mutual shadowing. *IEEE, Transactions on Geoscience and Remote Sensing*, Vol. 30, pp. 276-292.
- Morel, A. Optical modeling of the upper ocean in relation to its biogenous matter content (case I waters), *Journal of Geophysical Research*, 93(C9), 10749-10768, 1988.
- Rahman and Dedieu, 1994; SMAC : a simplified method for the atmospheric correction of satellite measurements in the solar spectrum", *Int. J. Remote Sensing*, 1994, vol.15, no.1, 123-143
- Ross, J.K. (1981). The radiation regime and architecture of plant stands, Dr W Junk, The Hague.
- Schaaf, CB, Gao, F, Strahler, AH, Lucht, W, Li, XW, Tsang, T, Strugnell, NC, Zhang, XY, Jin, YF, Muller, JP, Lewis, P, Barnsley, M, Hobson, P, Disney, M, Roberts, G, Dunderdale, M, Doll, C, d'Entremont, RP, Hu, BX, Liang, SL, Privette, JL, Roy, D (2002). "First operational BRDF, albedo nadir reflectance products from MODIS". *Remote Sensing of environment*, 83(2-Jan), 135-148.

1.1.4 Acronyms

6SV	Second Simulation of a Satellite Signal in the Solar Spectrum, Vector
AATSR	Advanced Along Track Scanning Radiometer
ADEOS	Advanced Earth Observation Satellite
AERONET	AErosol RObotic NETwork
ASTR	Along Track Scanning Radiometer

BRDF	Bidirectional Reflectance Distribution Function
Cal/Val	CALibration and VALidation
CEOS	Committee on Earth Observation Satellites
CNES	Centre National d'Etudes Spatiales
DIMITRI	Database for Imaging Multispectral Instruments and Tools for Radiometric Intercomparison
DN	Digital Number
DTM	Digital Terrain Model
ENVISAT	ENVIronment SATellite
EO	Earth Observation
ESA	European Space Agency
EUMETSAT	European Organisation for the Exploitation of Meteorological Satellites
GSICS	Global Space-based Inter-calibration System
IVOS	Infrared and Visible Optical Sensors
LandNet	Land Network
MERIS	Medium Resolution Imaging Spectrometer
MISR	Multi-angle Imaging SpectroRadiometer
MODIS	Moderate Resolution Imaging Spectroradiometer
NASA	National Aeronautics and Space Administration
NOAA	National Oceanic and Atmospheric Administration
OLCI	Ocean and Land Color Instrument
PARASOL	Polarization & Anisotropy of Reflectances for Atmospheric Sciences coupled with Observations from a Lidar
POLDER	POLarization and Directionality of the Earth's Reflectances
QA4EO	Quality Assurance Framework for Earth Observation
RADTRAN	Radiative Transfer
RIM	Radiometric Instrument Model
RTM	Radiative Transfer Model
SADE	Structure d'Accueil de Données d'Etalonnage
SWIR	Short Wave Infra-Red
TOA	Top Of Atmosphere
VGT	VEGETATION
VICaSEOOS	Vicarious Calibration System for Earth Observation Optical Sensors
VIS	VISible
WG	Working Group
WGCG	Working Group on Calibration and Validation

2 Introduction

This Algorithm Theoretical Basis Document describes the algorithm used to monitor the multitemporal calibration of satellite sensors using stable terrestrial sites. In particular, this document identifies sources of input data, both satellite and auxiliary data. It provides the physical theory and mathematical background underlying the use of this information in the method. It includes implementation details, and describes assumptions and limitations of the adopted approach.

This task is referred by task 3 of the SOW.

The software processes images acquired over the sites by ATSR-2, AATSR, MODIS/Aqua, MERIS, VEGETATION, and PARASOL instruments.

3 Algorithm overview

3.1 Principle of the method

The deserts are stable targets that are used for a long time for monitoring the radiometric stability of sensors on board satellite. Their temporal instability without atmospheric correction has been determined to be less than 1–2% over a year.

A list of selected sites has been identified in Sahara desert by several calibration teams; Holben et al., 1990; Kaufman and Holben, 1993; Cosnefroy et al., 1996, for instance. The reference list of Cosnefroy et al., 1996 accounts for 20 sites. Selection has been performed using Meteosat-4 data for the period July 1989–January 1990 to identify 100×100 km² areas with a relative spatial uniformity of less than 3%. These sites are monitored for more than 20 years and their characteristics have been described in terms of spectral and temporal variability.

Desert sites are large sites (1° x 1°). Among the 20 sites, one located in Libya is endorsed by the CEOS. The site is named Libya 4. Its location is [28.05 29.05E, 22.89-23.89 N]. The site is composed of dunes at multiple scales as it can be seen on the figure below.

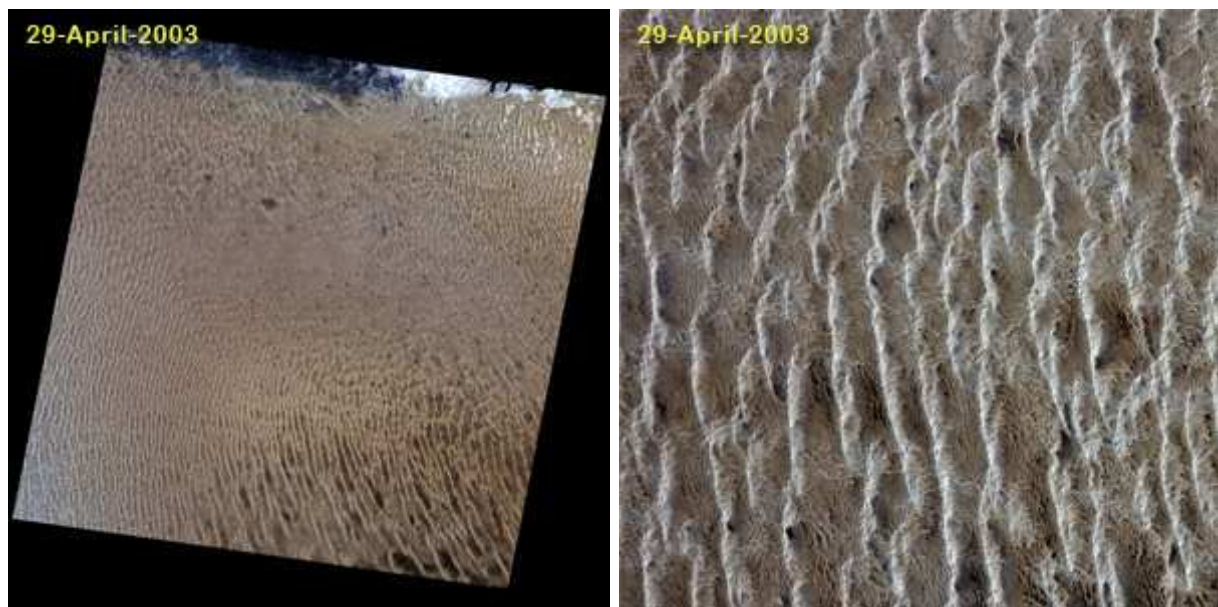


Figure 1: Libya 4 site seen by ETM (ETM+ Bands 321), source USGS.

The stability of the surface reflectance is the property that is used for developing the method. As the site is radiometrically stable, any change in the reflectance is attributed to the temporal change of the instrument's sensitivity.

Furthermore, these sites have been used to intercalibrate different sensors. But the method is not implemented in the frame of the project.

The principle of the method is to compare the measurements provided by the sensor above the desert site to a simulation of the top-of-atmosphere reflectance (Eq. 1). This ratio is computed

for all acquisitions and monitored on a large period of time to detect possible change in sensor radiometry.

$$\Delta\rho = \frac{\rho_{TOA}^{Measured}}{\rho_{TOA}^{Simulated}} \quad \text{Eq. 1}$$

In this ATBD, we will describe the method implemented to monitor the temporal variability of this ratio.

3.1.1 Method

3.1.1.1 Stability monitoring

Desert calibration method relies on the comparison between TOA reflectances (corrected for gaseous absorption) measured by the sensors available in DIMITRI database and the modelled TOA reflectances. The desert calibration is based on the monitoring of the stability of ρ_{toa} . A surface model is coupled to the atmosphere to simulate the TOA reflectance using RTM.

The TOA reflectance, normalised to the gaseous transmission, is modelled by the following expression:

$$\rho_{toa} = \rho_{atm} + \frac{T_{atm}^{\downarrow} \rho_g T_{atm}^{\uparrow}}{(1 - s_{atm} \rho_s)} \quad \text{Eq. 2}$$

The comparison of the modelled to the measured reflectance over time provided the assessment of the calibration.

In the method, the TOA reflectance values are estimated using the SMAC method (Rahman and Dedieu, 1994; Berthelot and Dedieu, 2000). The input of the SMAC method is the same as the input of the 6SV radiative transfer code.

In this case, simulated TOA reflectances values are determined by three types of factors:

- surface properties
 The surface properties of desert sites can be described well with a BRDF model. Several models are available.
- atmospheric conditions
 Even aerosols loadings are unknown, their influence is low because an increase of the aerosol loading results in an increase of the atmospheric reflectance but decreases the atmospheric transmittance and therefore the surface contribution. The two opposite effects are well balanced. A mean value is be used.
- Observation conditions including solar zenith angle, view zenith angle and relative azimuth angle.

As SMAC is an analytical method, the comparison of the measured TOA against the simulated one provides the estimation of the relative difference. The evaluation of the sensor radiometry is defined by the ratio of the measured reflectance over the estimated one (Eq. 1)

3.1.1.2 Multitemporal monitoring

The goal of multi-temporal calibration is to monitor the stability and variations of the sensors responses over time. The temporal variations of the ratio are monitored regularly against time for a long period. A function is fitted to estimate the variability against time.

3.1.2 Modelling

3.1.2.1 SMAC

SMAC (Simplified Method for Atmospheric Correction) initially developed by Rahman and Dedieu (1994) is a method which allows correcting atmospheric effects of satellite data time series based on 5S radiative transfer model. The method has been upgraded by Berthelot and Dedieu, (1997) based on 6Sv41 radiative transfer model and used for the correction of atmospheric effects of VEGETATION data in an operational processing line (at CTIV). It is also added as a processor in the ESA BEAM toolbox to correct MERIS L1B data from atmospheric effects over land.

The atmospheric parameters are estimated using a set of equations which described analytically the absorption and scattering of molecules and aerosols in the atmosphere. The code is generic. Only the set of coefficients applied on these equations is depending on the spectral band. These coefficients are computed for a selected type of aerosol and one type of atmosphere.

The performance of SMAC/6S atmospheric reflectance estimation has been evaluated by computing the root mean square error (rmse) and the maximum absolute or relative error with respect to the 6S reference for SMAC. More than 50.000 simulations including extreme variations of the input parameters have been made to get the following results.

The root mean square error (rmse) is used to assess the performance of the method. It is expressed in reflectance unit. Rmse in blue band is around 0.007. It decreases to 0.002 in the NIR bands, and 0.001 in the SWIR.

3.1.2.2 BRDF

The surface properties of Libya4 site are described with a BRDF model. We choose to model the bidirectional reflectance of the surface using a reflectance model developed by MODIS team (Schaaf et al, 2002). The MODIS BRDF/Albedo algorithm is a linear BRDF model which relies on the weighted sum of an isotropic parameter and two functions (or kernels) of viewing and illumination geometry to determine reflectance. One of these kernels, $K_{vol}(\theta_s, \theta_v, \phi, \lambda)$, is derived from volume scattering radiative transfer models (Ross, 1981) and the other, $K_{geo}(\theta_s, \theta_v, \phi, \lambda)$, from surface scattering and geometric shadow casting theory (Li and Strahler, 1992).

$$R(\theta_s, \theta_v, \phi, \lambda) = f_{iso}(\lambda) + f_{vol} \cdot K_{vol}(\theta_s, \theta_v, \phi, \lambda) + f_{geo} \cdot K_{geo}(\theta_s, \theta_v, \phi, \lambda) \quad \text{Eq. 3}$$

The MODIS BRDF/albedo product provides with the three coefficients used to estimate the surface reflectance. f_{iso} , f_{vol} and f_{geo} parameters are referred by K1, K2, K3 in the following.

3.1.2.2.1 KERNEL description

The BRDF model kernel K_{vol} (also called RossThick kernel) is given by:

$$K_{vol}(\theta_s, \theta_v, d\phi) = \frac{(\pi/2 - \xi) \cos \xi + \sin \xi}{\cos(\theta_s) + \cos(\theta_v)} - \frac{\pi}{4} \quad \text{Eq. 4}$$

Where ξ is the scattering angle, given by

$$\cos \xi = \cos(\theta_s) \cos(\theta_v) + \sin(\theta_s) \sin(\theta_v) \cos d\phi \quad \text{Eq. 5}$$

The BRDF model kernel K_{geo} (also called LiSparse kernel) is given by:

$$K_{geo}(\theta_s, \theta_v, d\phi) = O(\theta_s, \theta_v, d\phi) - \sec(\theta_s) - \sec(\theta_v) + \frac{1}{2}(1 + \cos(\xi))\sec(\theta_s)\sec(\theta_v) \quad \text{Eq. 6}$$

Where

$$O(\theta_s, \theta_v, d\phi) = \frac{1}{\pi}(t - \sin t \cos t)(\sec(\theta_s) + \sec(\theta_v)) \quad \text{Eq. 7}$$

With

$$\cos t = \frac{2\sqrt{D^2 + (tg(\theta_s)tg(\theta_v)\sin(d\phi))^2}}{\sec(\theta_s) + \sec(\theta_v)} \quad \text{Eq. 8}$$

And with

$$D = \sqrt{tg^2(\theta_s) + tg^2(\theta_v) - 2tg(\theta_s)tg(\theta_v)\cos(d\phi)} \quad \text{Eq. 9}$$

3.1.2.2.2 MCD43B1 product description

The MODIS BRDF/Albedo Model Parameters product (MCD43B1) contains three-dimensional (3D) data sets providing users with weighting parameters for the anisotropy models used to derive the Albedo and BRDF products. The models support the spatial relationship and parameter characterization best describing the differences in radiation due to the scattering (anisotropy) of each pixel, relying on multi-date, atmospherically corrected, cloud-cleared input data measured over 16-day periods (Source MODIS).

Both Terra and Aqua data are used in the generation of this product, providing the highest probability for quality input data and designating it as an MCD, meaning Combined, product.

Data are available at 1km, which is an average of the 500m values. The products are produced every 8 days with 16 days of acquisition (i.e., production period 2001001 includes acquisition between Days 001 and 016, production period 2001009 includes acquisition between Days 009 and 024). 46 products are available per year.

MCD43B1 product supply spectral MODIS channels 1–7 BRDF model parameters used to reconstruct the entire surface BRDF and compute the directional reflectance at any view or solar zenith angle desired.

Coefficients have been extracted over Libya 4 from 2008 to 2012. An example is reported in the figure below for all bands.

Table 3: MODIS spectral band order

Band	Bandwidth (nm)
1	620 - 670
2	841 - 876
3	459 - 479
4	545 - 565
5	1230 - 1250
6	1628 - 1652
7	2105 - 2155

The spatial, variability of each coefficient in all MODIS band is represented hereafter for one date (2011, Julian day 180).

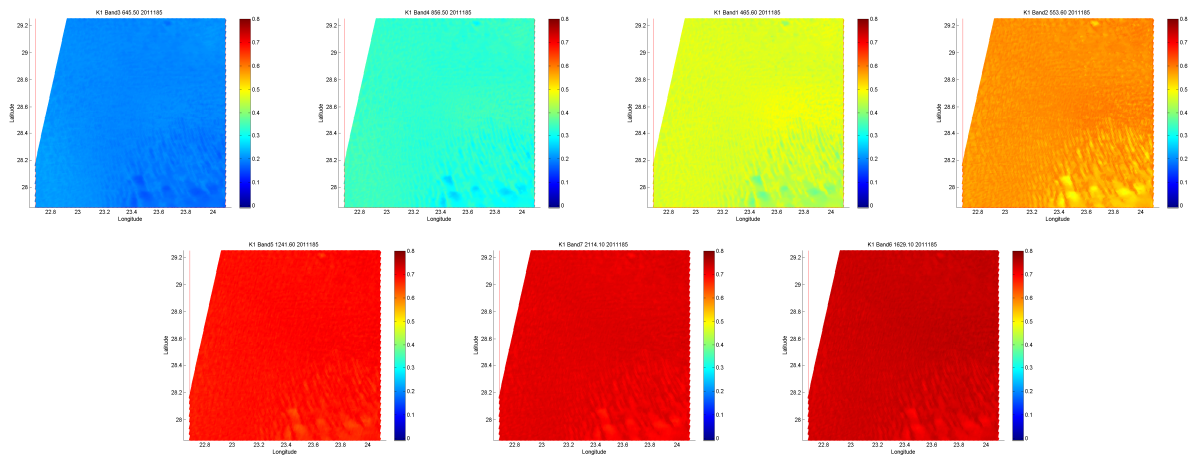


Figure 2: K1 coefficient- Synthesis of June, Julian day 180, 2011

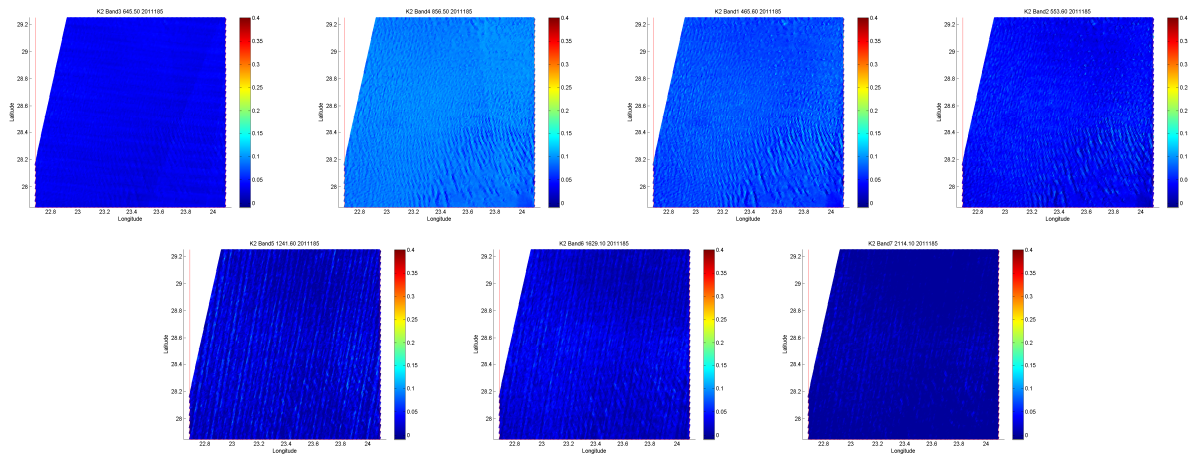


Figure 3: K2 coefficient- Synthesis of June, Julian day 180, 2011

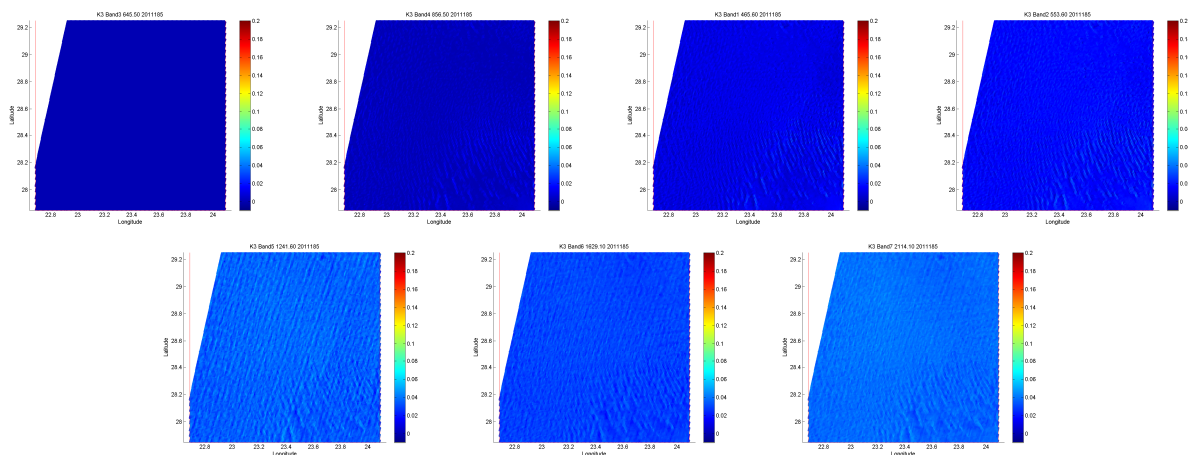


Figure 4: K3 coefficient- Synthesis of June, Julian day 180, 2011

3.1.2.3 Atmosphere characteristics

The desert aerosol model is used with an aerosol optical thickness set to 0.2 at 550 nm.

3.2 Implementation description

3.2.1 Overall steps

This paragraph provides with the overall steps that have to be done to estimate the ratio of measured out to simulated reflectance .

- 1) Read the database and select images acquired in the desert site.

For each selected date (loop)

- 2) Read the TOA reflectances of clear pixels acquired into the site footprint for the selected date.
- 3) Read auxiliary data
 - 3.1) Water vapour content
 - 3.2) Ozone content
- 4) Check Pixels selection test
 - 4.1) Select valid pixels
 - 4.2) Select clear pixels
 - 4.3) Select scenes for which cloud coverage is less than 10%
- 5) Correct TOA reflectances from gaseous absorption
- 6) Read BRDF model coefficient interpolated at the date of the acquisition in the 7 MODIS bands
- 7) Simulate the BRDF in MODIS band for the geometry of the sensor
- 8) For all sensors except MODIS
 - 8.1) Interpolate spectrally the surface reflectance for the spectral band of the sensor
- 9) Estimate the TOA reflectance in the sensor bands using SMAC
- 10) Estimate the reflectance ratio in the all bands

3.2.2 Detailed steps

3.2.2.1 Input data selection

DIMITRI data ingestion module allows to extract for each acquisition the area which contains the desert site. One file is written for one acquisition. According to the period selected by the user, these files are read and used as input of the method.

The output file of the ingestion module contains the following information:

- Latitude;
- Longitude;
- Zenith and azimuth solar angles;
- Zenith and azimuth view angles;
- TOA reflectances in all channels;
- Cloud mask ;

3.2.2.2 Auxiliary data extraction

Water vapour content, ozone content and wind speed are extracted from ERA dataset for the location of the site. The data are provided each 6 hours. A linear interpolation is performed to estimate the different content at the hour of acquisition.

3.2.2.3 Pixel selection

The selection of pixels is the first step of the processing. The selection checks that there are:

- Valid pixels;
- Clear pixels;
- Less than 10% of clouds in the site.

If the following criteria are not validated, the method is not applied.

3.2.2.4 Correct TOA reflectances from gaseous transmission

The gaseous transmission has been estimated using SMAC formulation.

Analytical formulation is used to simulate the gaseous transmission from the air mass, gaz content (water vapour content, ozone content) and surface pressure. The formulation has been developed first by Rahman and Dedieu, (1996), then improved by Berthelot and Dedieu (2000). SMAC coefficient database has been developed for all optical sensors on orbit up to 2008 by B. Berthelot and is made available for free on CESBIO web site. The coefficients are estimated for H₂O, O₃, O₂, CO₂, CH₄, NO₂, CO gaz.

- Input for total gaseous transmission estimation is :
 - Solar zenith angle
 - View zenith angle
 - Water vapour content
 - Ozone content
 - Pressure
 - SMAC coefficients for all bands
- Output is :
 - Total Gazeous transmission.

3.2.2.5 RTM Solar Irradiance correction

The comparison of the TOA reflectance to the simulated one is not direct unless the transformation of radiances to reflectances is performed using the same solar irradiance reference. Indeed, the sensors record raw digital numbers (DN) that are related to the radiances with a sensor radiometric model that can be more or less complex. Once all parameters of this radiometric model estimated, the radiance can be estimated from the measured digital numbers. Then, the TOA reflectances are computed from radiances using the conversion:

$$\rho_{TOA}^k = \frac{\pi L^k}{E_{os}^k \left(\frac{d_o}{d}\right)^2 \cos(\theta_s)} \quad \text{Eq. 10}$$

Where k refers to the spectral band, E_{os} is the solar extraterrestrial irradiance in the spectral band k, (d_o/d) is the ratio of Sun-Earth distance at the acquisition date to the mean Sun-Earth distance, and θ_s is the solar zenith angle.

The use of a RTM allows to simulate the apparent reflectance at the satellite level. This reflectance is modelled by:

$$\rho_{6S-TOA}^k = \frac{\pi L^k}{E_{os-6S}^k \left(\frac{d_o}{d}\right)^2 \cos(\theta_s)} \quad \text{Eq. 11}$$

Where for this case E_{os-6S} is the 6S solar extraterrestrial irradiance in the spectral band k. 6S solar irradiance reference is Neckel and Labs, 1984.

In order to compare both TOA reflectances, the measured reflectance has to be weighted by the ratio of the solar extraterrestrial irradiance

$$\rho_{6S-TOA}^k = \rho_{TOA}^k \times \frac{E_{os}^k}{E_{os-6S}^k} \quad \text{Eq. 12}$$

The 6S solar irradiances are reported hereafter for each spectral band in a table where the solar irradiance used for the transformation of radiances to radiances are also provided. The corrective factor is indicated in the last column.

Table 4: Solar irradiance

Sensor	Band number	Central wavelength [nm]	E_{os} sensor (W/m ²)	E_{os-6S} (W/m ²)	E_{os} / E_{os-6S}
MODIS	1	645	1578.11	1603.89	0.984
MODIS	2	858.5	971.74	992.78	0.979
MODIS	3	469	2058.78	2012.55	1.023
MODIS	4	555	1838.69	1859.45	0.989
MODIS	5	1240	454.67	453.66	1.002
MODIS	6	1640	239.77	237.82	1.008
MODIS	7	2130	98.85	95.25	1.038
PARASOL	1	443	1891.16	1897.41	0.997
PARASOL	2	490	1928.39	1935.50	0.996
PARASOL	3	565	1843.69	1842.30	1.001
PARASOL	4	670	1527.45	1532.73	0.997
PARASOL	5	763	1225.40	1229.75	0.996
PARASOL	6	765	1228.45	1232.41	0.997
PARASOL	7	865	980.89	980.40	1.000
PARASOL	8	910	885.09	929.03	0.953
PARASOL	9	1020	712.50	726.33	0.981
MERIS	1	412.5	1716.09	1735.08	0.989
MERIS	2	442.5	1880.34	1858.00	1.012
MERIS	3	490	1929.82	1924.68	1.003
MERIS	4	510	1930.42	1916.12	1.007
MERIS	5	560	1804.47	1845.70	0.978
MERIS	6	620	1652.05	1700.73	0.971
MERIS	7	665	1532.81	1547.51	0.991

MERIS	8	681.25	1473.30	1495.47	0.985
MERIS	9	708.75	1409.03	1394.20	1.011
MERIS	10	753.75	1267.02	1262.78	1.003
MERIS	11	760.625	1255.55	1242.03	1.011
MERIS	12	778.75	1178.17	1192.53	0.988
MERIS	13	865	959.12	972.21	0.987
MERIS	14	885	930.56	975.05	0.954
MERIS	15	900	896.15	943.92	0.949
AATSR	1	560	1819.54	1853.11	0.982
AATSR	2	660	1521.89	1546.01	0.984
AATSR	3	862	950.68	971.14	0.979
AATSR	4	1593	254.48	253.03	1.006
VGT	1	460	1963.40	1972.01	0.996
VGT	2	670	1570.30	1551.73	1.012
VGT	3	825	1045.60	1058.47	0.988
VGT	4	1640	234.70	228.24	1.028
ATSR2	1	554			
ATSR2	2	658			
ATSR2	3	864			
ATSR2	4	1608			

3.2.2.6 Read BRDF model coefficient interpolated at the date of the acquisition in the 7 MODIS bands

The BRDF coefficients have been beforehand extracted from the MODIS BRDF product on the site location. The 21 coefficients (3 K x 7 spectral bands) are interpolated linearly at the date of acquisition from the product.

3.2.2.7 Simulate the BRDF in the 7 MODIS bands for the geometry of the sensor

The BRDF is computed using the three coefficients and the model in the geometry configuration of the acquisition.

3.2.2.8 Spectral interpolation

This step is applied only for all sensors except MODIS. The surface reflectance is interpolated in the spectral bands of the sensor using the surface reflectance estimated in the previous step using a spline function.

3.2.2.9 TOA reflectance estimation

The SMAC method is used to simulate the TOA reflectance (normalised to the gaseous transmission) using the atmosphere characteristics and the solar and view geometry of the acquisition.

3.2.2.10 $\Delta\rho$ estimation in the all band

The ratio of measured TOA reflectances out to simulated TOA reflectances is computed for all the bands.

$$\Delta\rho = \frac{\rho_{toa}^{measured}}{\rho_{toa}^{estimated}} \text{ Eq. 13}$$

As the algorithm is applied on a pixel per pixel basis, a statistical analysis on the ratio is made to remove outliers. Mean and standard deviation of the ratio are estimated and values out of three σ are removed.

3.2.2.11 Statistical analysis of the sensor radiometry

The last step consists in averaging the values of the ratio obtained for one acquisition and monitor it with time.

$$\overline{\Delta\rho} = \text{mean}\left(\frac{\rho_{TOA}^{Measured}}{\rho_{TOA}^{Simulated}}\right) \text{ Eq. 14}$$

3.2.3 Auxiliary data

3.2.3.1 Thresholds

The following threshold has been defined:

Table 5: Threshold used to select data

Name	Threshold value
Maximum coverage Cloud	10%

3.2.3.2 Filtered BRDF

The analysis of the BRDF model reports that the temporal variability is very noisy from one date to another one. It appears that if not filtered clouds are present in one product used in the synthesis composition, the triplet coefficients is not stable and contains this cloud information both in amplitude and spatially.

The spatial variability of the coefficients highlights too much variability and the temporal variability of the coefficients appears very disturbed.

For instance, the following images are the coefficients K1 for three successive syntheses. We can observe that some residual clouds, not detected are present in the first two products, whereas the third one highlights a level of K0 different of the two previous one.

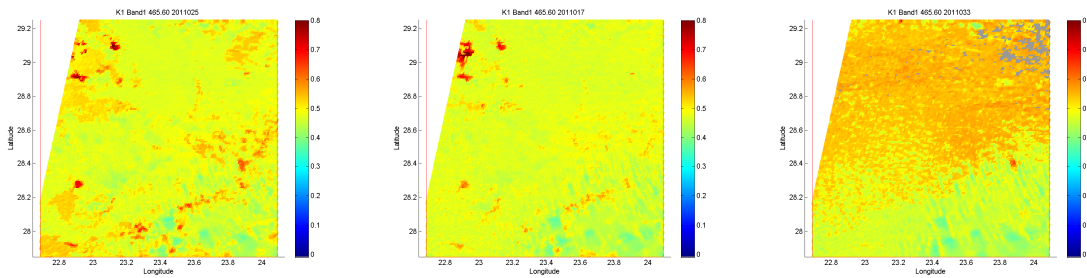


Figure 5: Variability of the K1 coefficient for three successive syntheses

This observation has led to apply a filter to remove the variability. A FFT has been chosen and apply on the five years of data to smooth the temporal profile.

The figure below shows the raw and smoothed profiles.

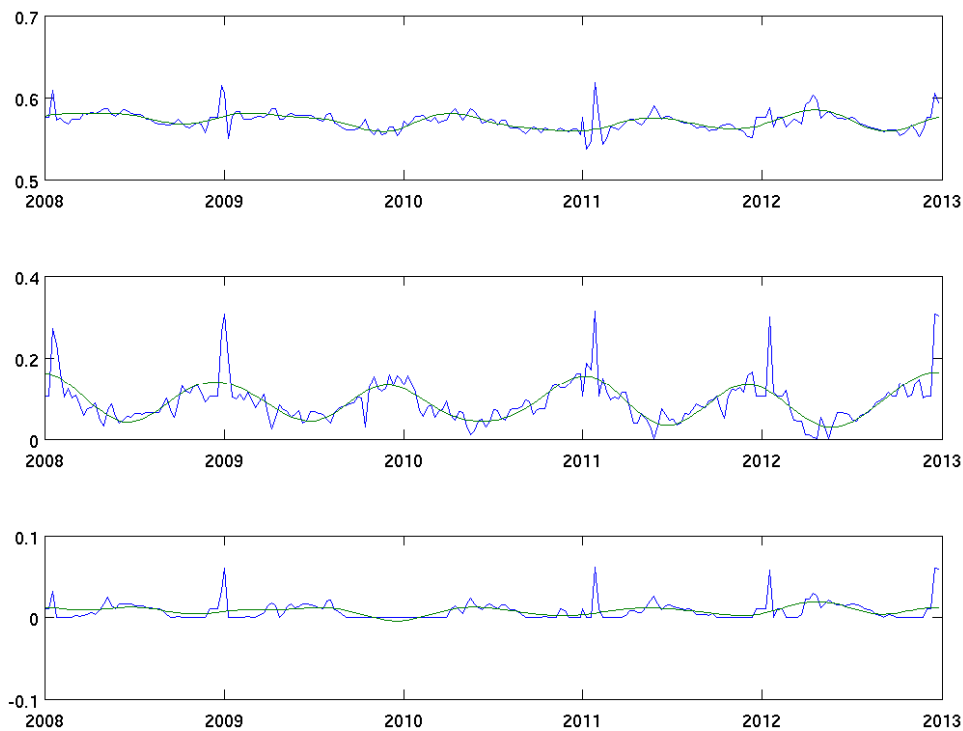


Figure 6: Temporal profile of K0, K1, K2 for the five years. The green line is the filtered profile.

Using these filtered data, the sensor radiometry monitoring could be performed only for years 2008 to 2012. This is a limitation at this date of the writing, but there are a few solutions to raise the limitation, such as downloading the overall MODIS products from 2002, or work on the BRDF product dataset to merge annual information using the 10 available years into a single product.

Remark: A few tests have already been performed to filter the data.

- The use of BRDF of one date, based on the assumption that the BRDF is stable
- The use of one year as reference for all the years processed.

The filtering using the FFT has been tested, but is opened to change.

3.2.4 Ancillary data

Water vapour content, ozone content and pressure are taken from the ERA interim datasets. ERA-Interim is a global atmospheric reanalysis from 1979 to present. Global atmospheric and surface parameters from 1 January 1979 to present, at T255 spectral resolution (~80 km) on 60 vertical levels are available. For this study, 6-hourly atmospheric fields on water vapour content, ozone content, and wins speed have been downloaded from 2001 to year 2012 from the ECMWF Data Server.

Table 6: Ancillary data needed in the DESERT method

Data	Source	Background
Water vapour content	ECMWF	
Ozone content	ECMWF	Climatology
Pressure	ECMWF	1013.25

4 Dataset analysis to monitor the sensor radiometry using desert site

4.1 Analysis of MODIS

4.1.1 Details of results for a single date

The following results and illustrations detail the estimation of the reflectance ratio for one date: MODIS acquisition of 04/01/2009. The illustration follows the implementation plan description in the previous section, step by step.

Read the database and select images

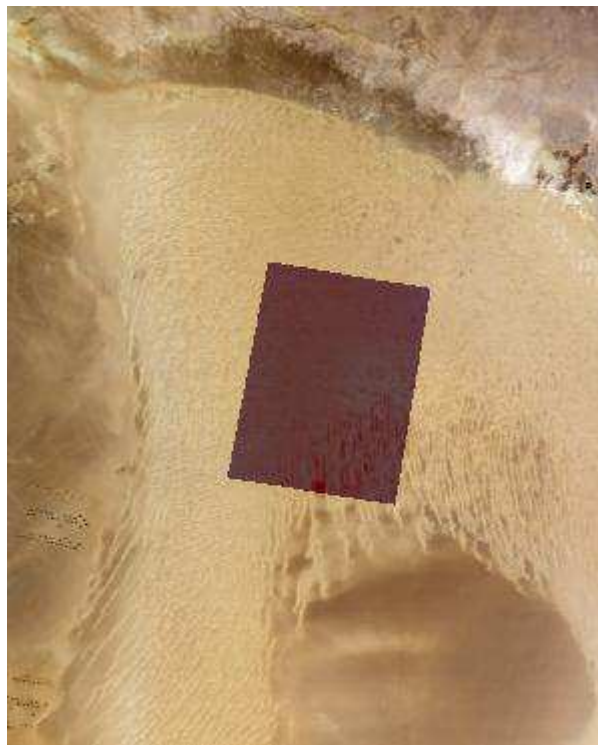


Figure 7: MODIS acquisition 04/01/2009 (Product MYD021KM.A2009004.1155.005.2009330144122.gscs_000500567696_hdf)

Read the TOA reflectances of clear pixels acquired into the site footprint for the selected date.

The TOA reflectance in the VIS and NIR channel (1 and 2) are represented below. This representation is shown in image coordinates (Column/Row).

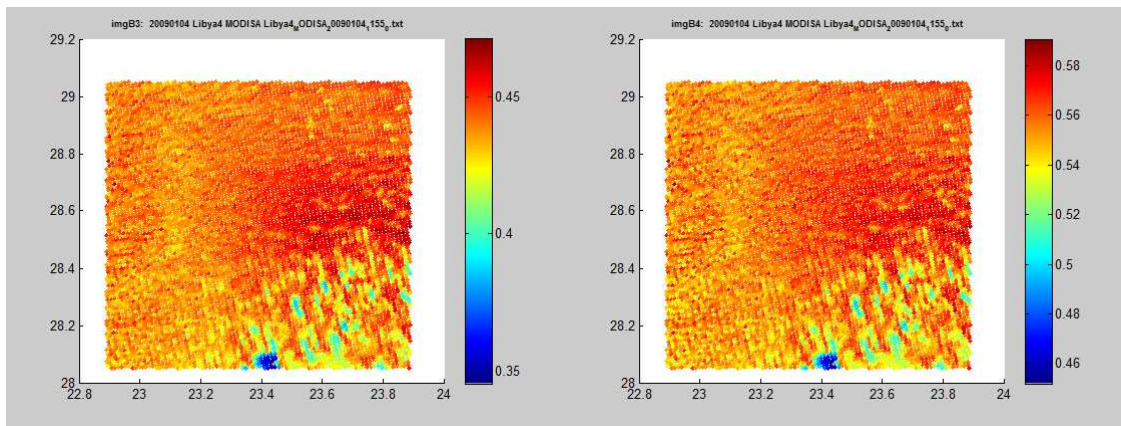


Figure 8: TOA reflectances in channels 1 and 2

Check Pixels selection test

- Select valid pixels
- Select clear pixels
- Select scenes for which cloud coverage is less than 10%

A mask of valid pixel is applied is computed from the acquisition. These data are flagged inside the products, and the information is conserved in the data extracted from the ingestion module. For MODIS acquisitions, the main channel which contains INVALID data is the SWIR (1.6µm) channel, but it happened that some saturation or other problem exists. These data are removed of the selected pixels by the pixel selection module. The mask is represented hereafter.

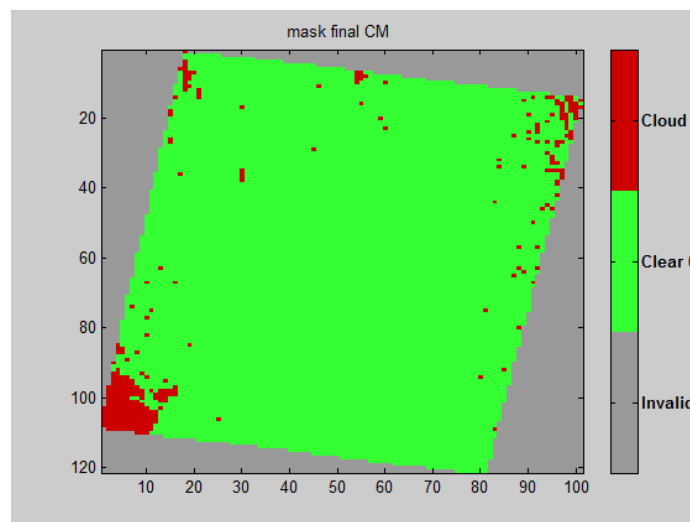


Figure 10: Cloud mask

Correct TOA reflectances from gaseous absorption

The comparison of TOA measurements to the simulation is performed on TOA reflectance normalized to gaseous absorption.

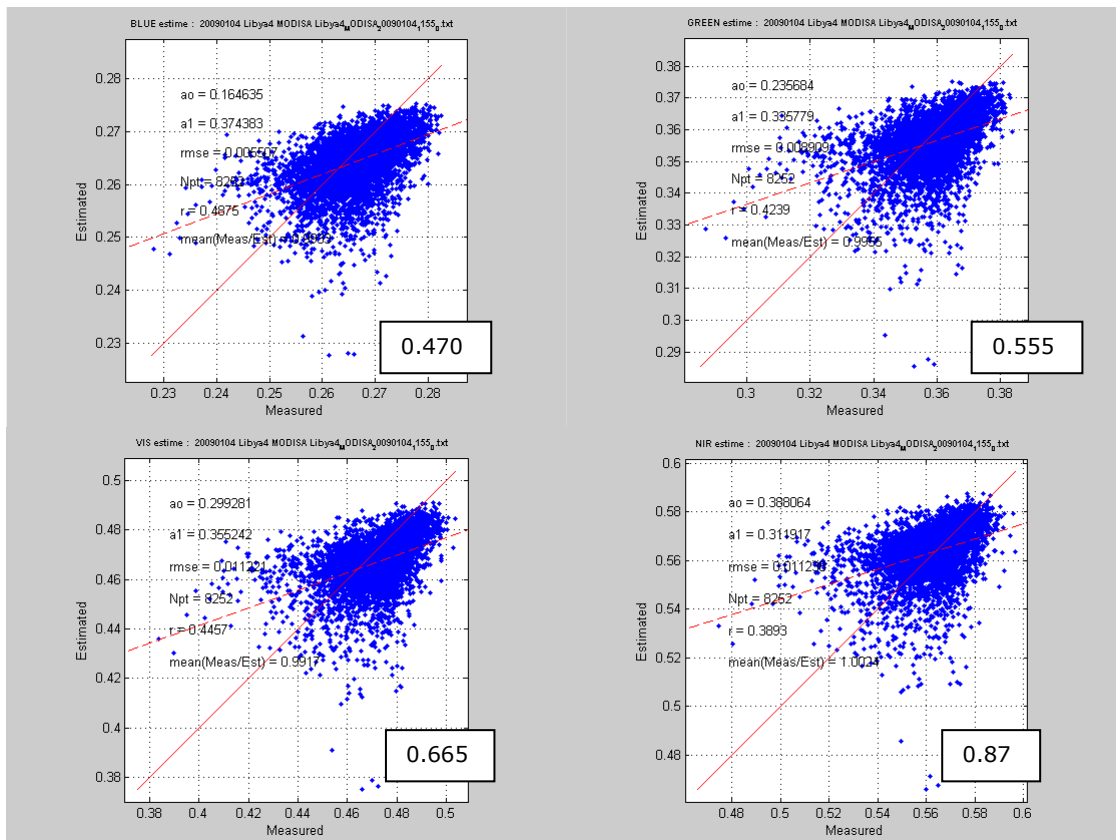
The SMAC method allows to estimate the gaseous transmission for the atmospheric content read from ERA data at the date of acquisition. These coefficients are provided for each spectral bands used in the method.

Estimate the TOA reflectance in the 7 MODIS bands using SMAC

The MODIS bands are referred in the report as follows:

Table 6: MODIS band name

Band number	Band name	Central wavelength (nm)
1	VIS	645
2	NIR	858.5
3	BLUE	469
4	GREEN	555
5	SWIR0	1240
6	SWIR	1640
7	SWIR2	2130



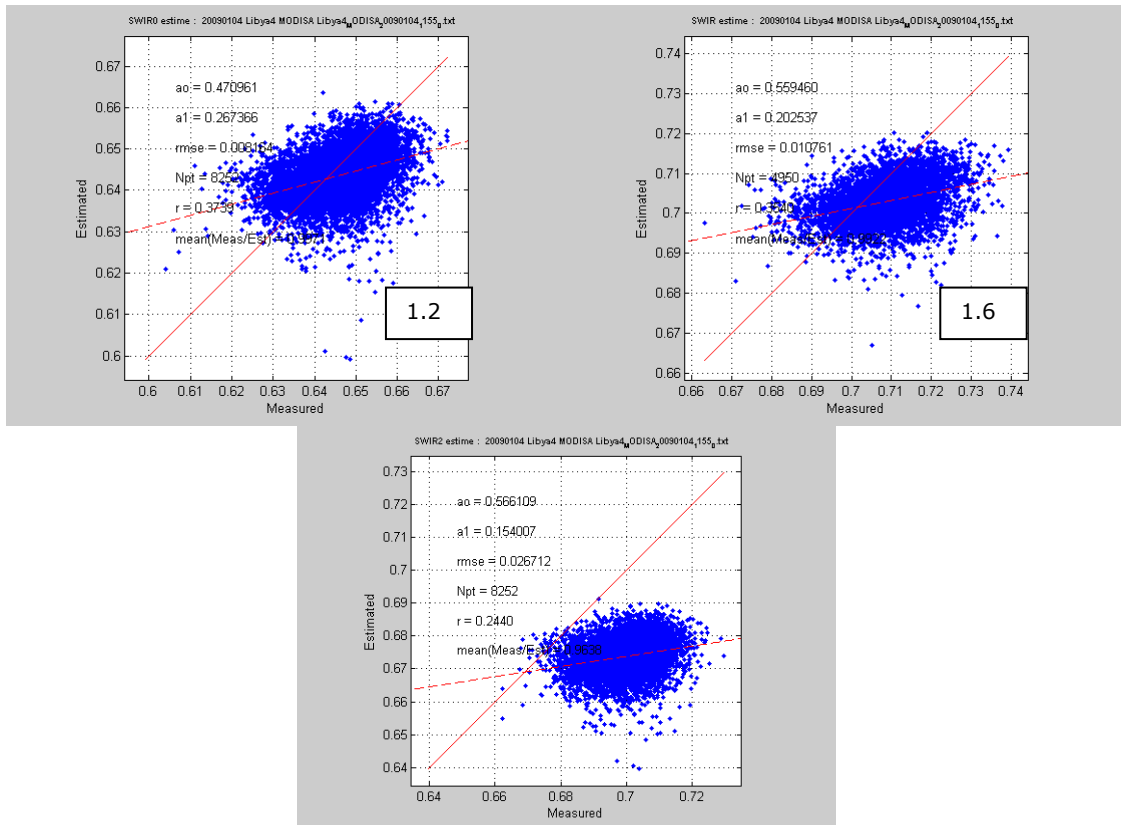


Figure 11: Scatterplot of simulated TOA reflectances versus measured TOA reflectances for all MODIS bands. Central wavelength in μm is indicated in a frame inserted in the figure.

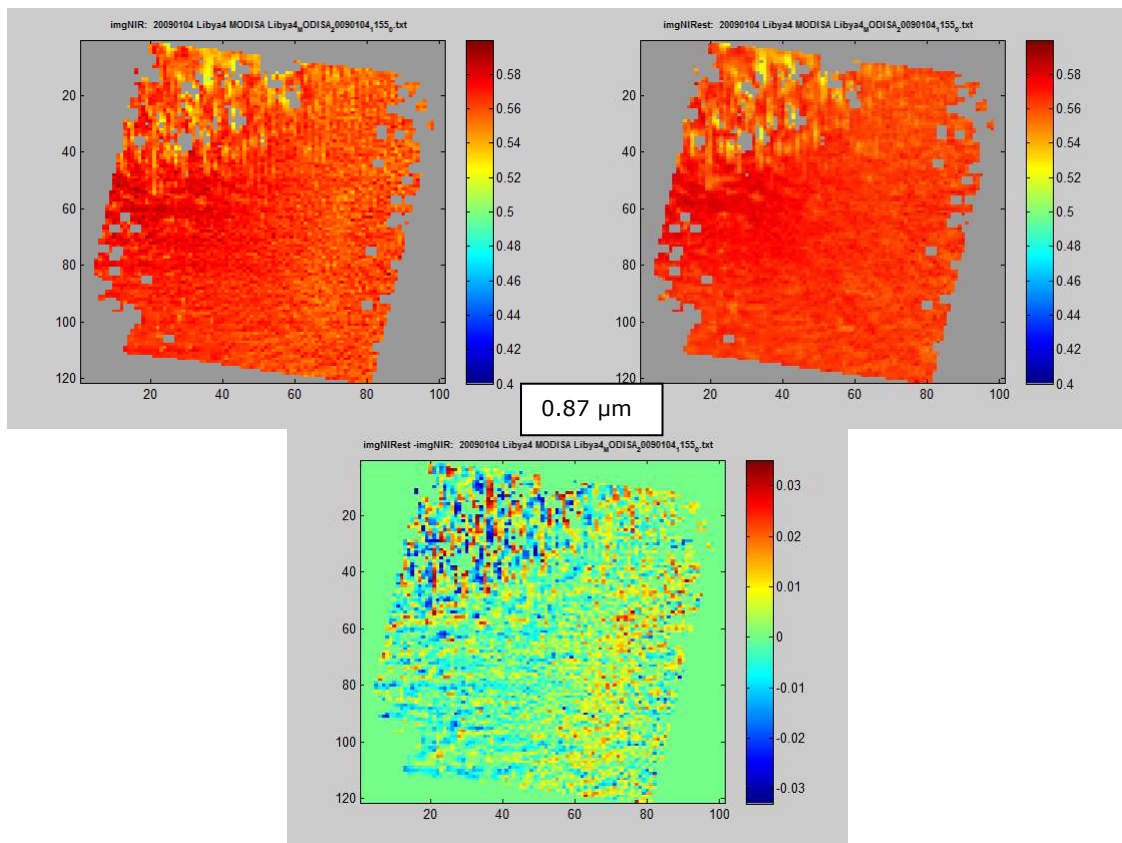


Figure 12: TOA reflectance in the NIR. Measured (top left), Simulated (top right), difference estimated minus measured (bottom).

Estimate the measured to simulated TOA reflectance ratio in the 7 MODIS bands

Once the simulated TOA reflectance estimated all the valid pixels, a map of the ratio is computed allowing to see the spatial variability and possible effects due to cloud edge. As an example, the map of reflectance ratio in the NIR channel is represented here after:

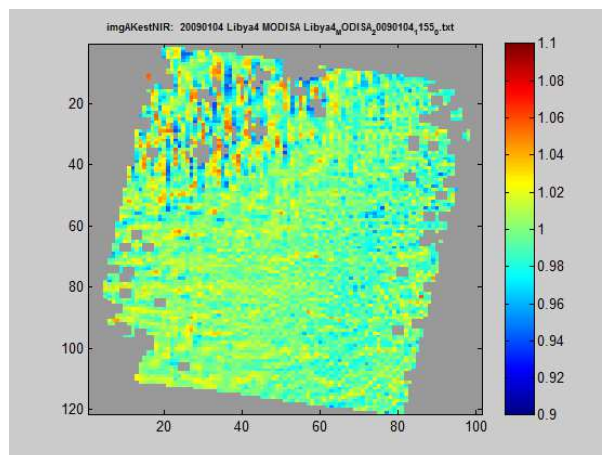


Figure 13: Map of the reflectance ratio in the NIR band

The histograms of the reflectance ratio in the seven bands are the following:

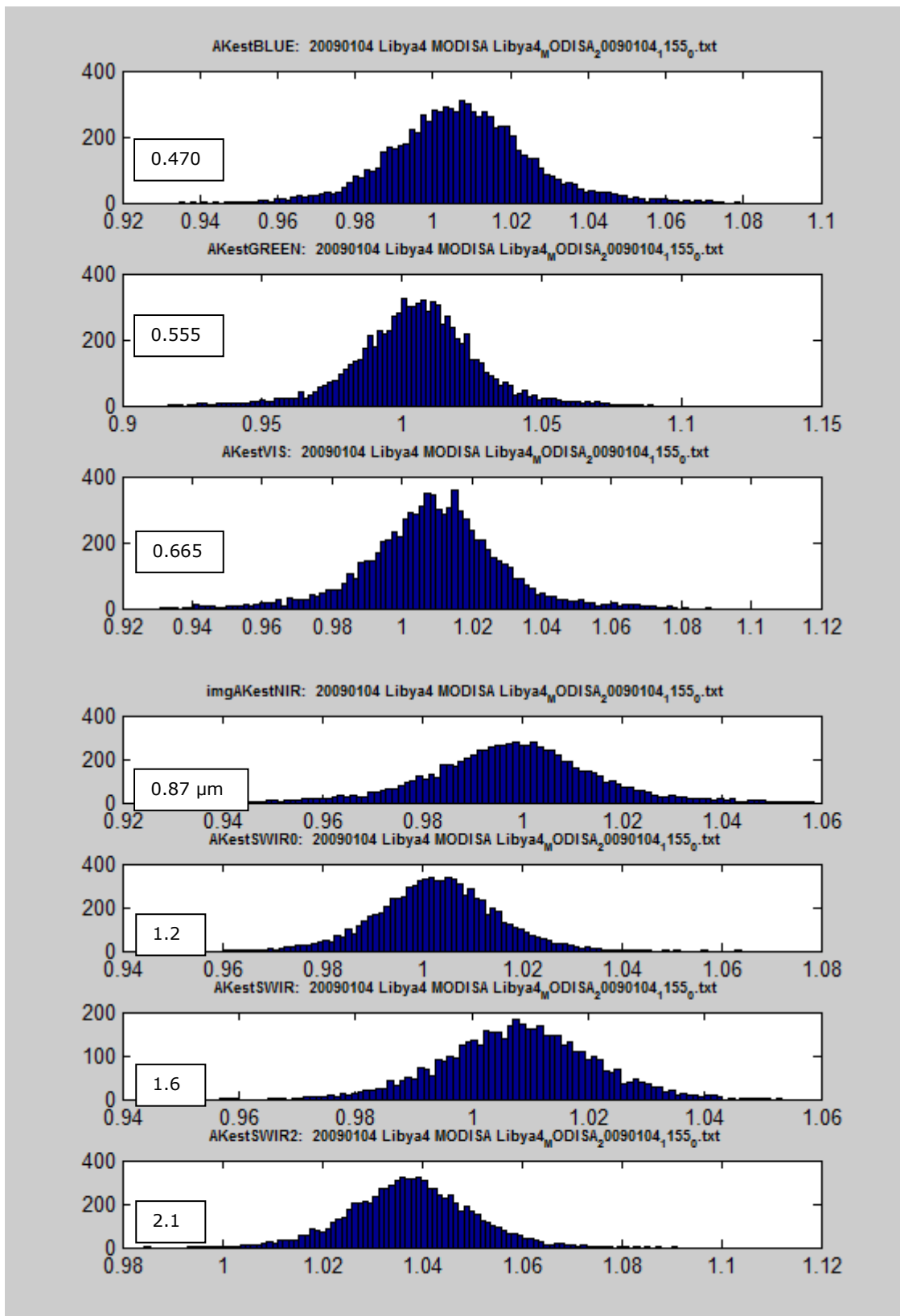


Figure 14: Ratio of Measured to Simulated TOA reflectance histograms. Central wavelength in μm is indicated in a frame inserted in the figure.

4.1.2 Multiyear results

The change in sensor radiometry is estimated by computing the mean of the measured to simulated TOA reflectances ratio for all available acquisitions. It is represented for the seven bands in the figures below from 2008 to 2011.

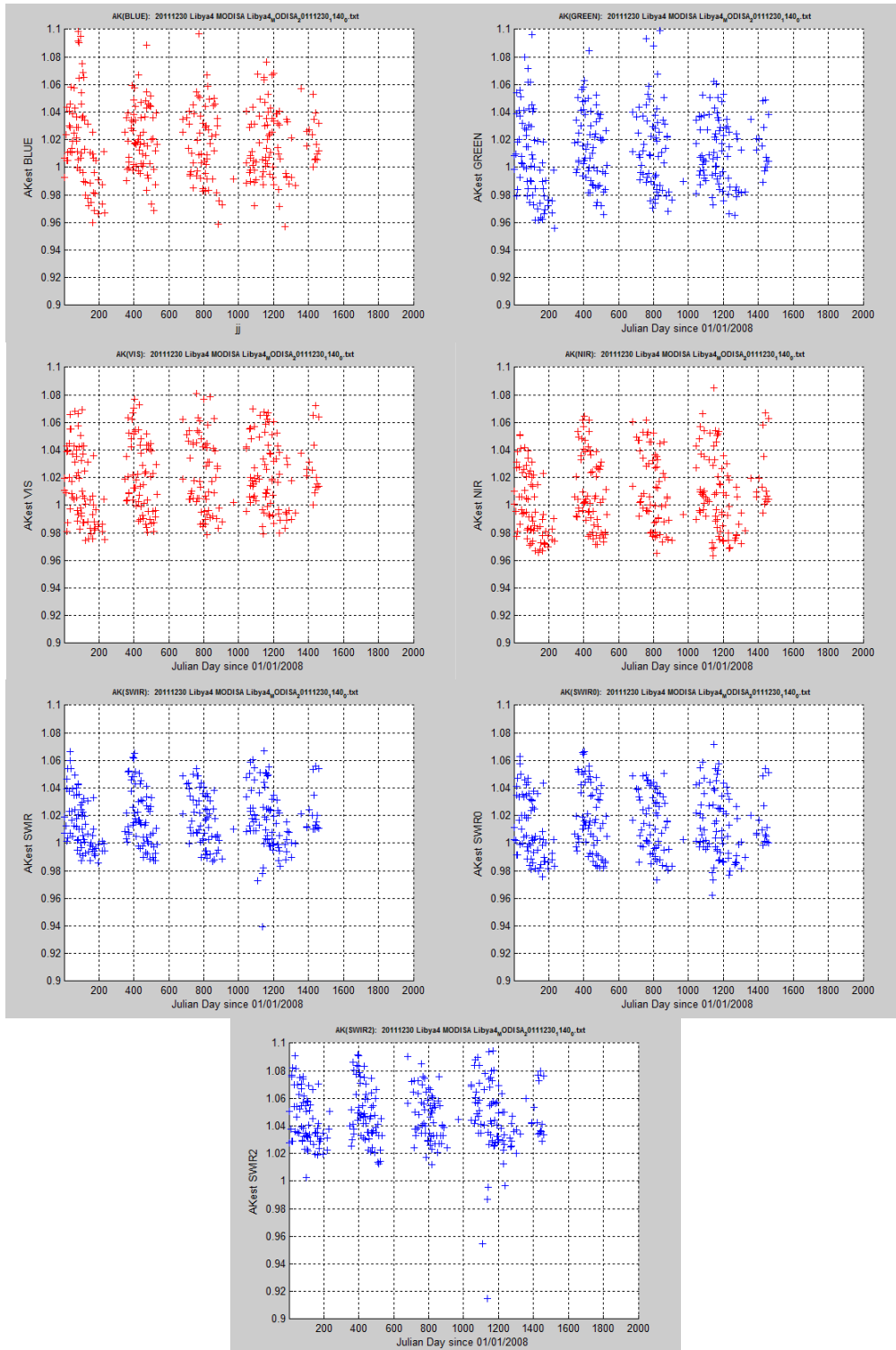


Figure 15: Temporal variability of the mean ratio between 2008 and 2011

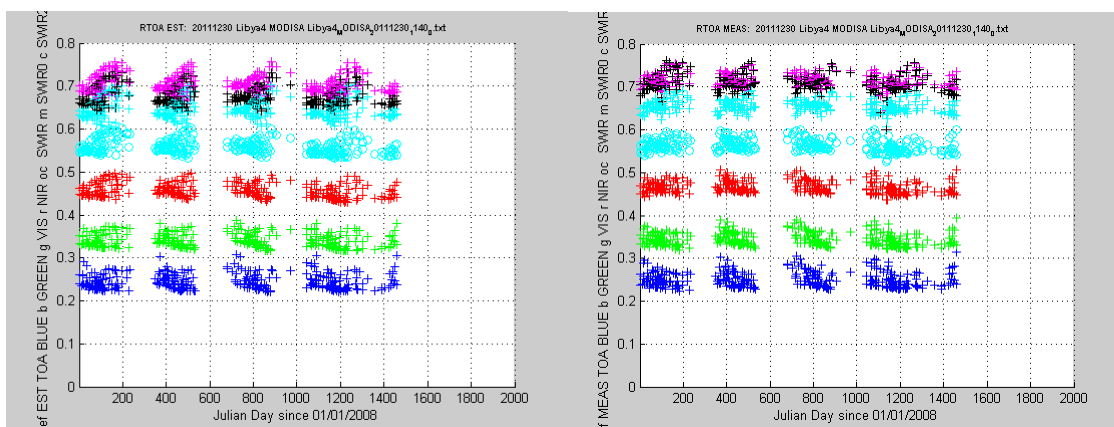
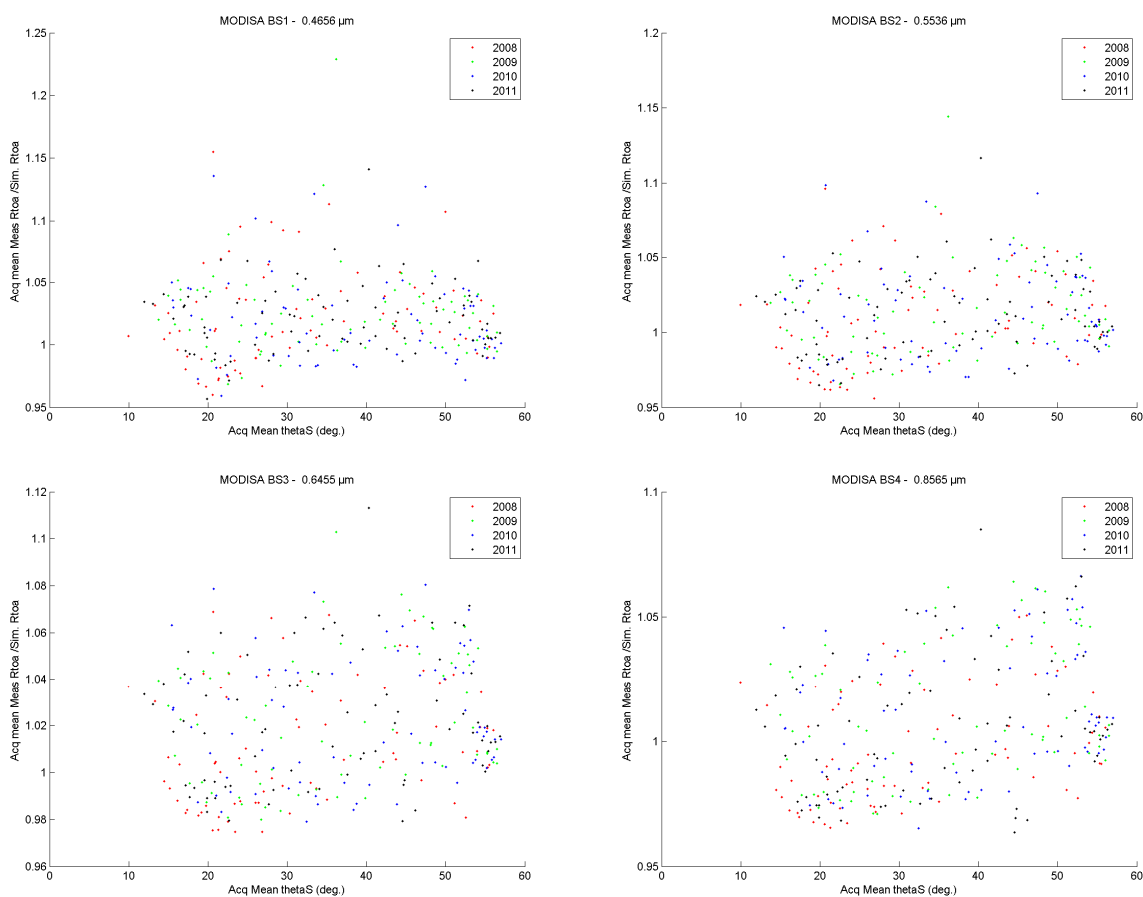


Figure 16: Temporal variability of the TOA reflectance (measured and simulated)

The variability of the ratio in the seven MODIS channels is plotted versus the mean solar zenith angle observed at the acquisition date. No trend is observed except in the SWIR channels.



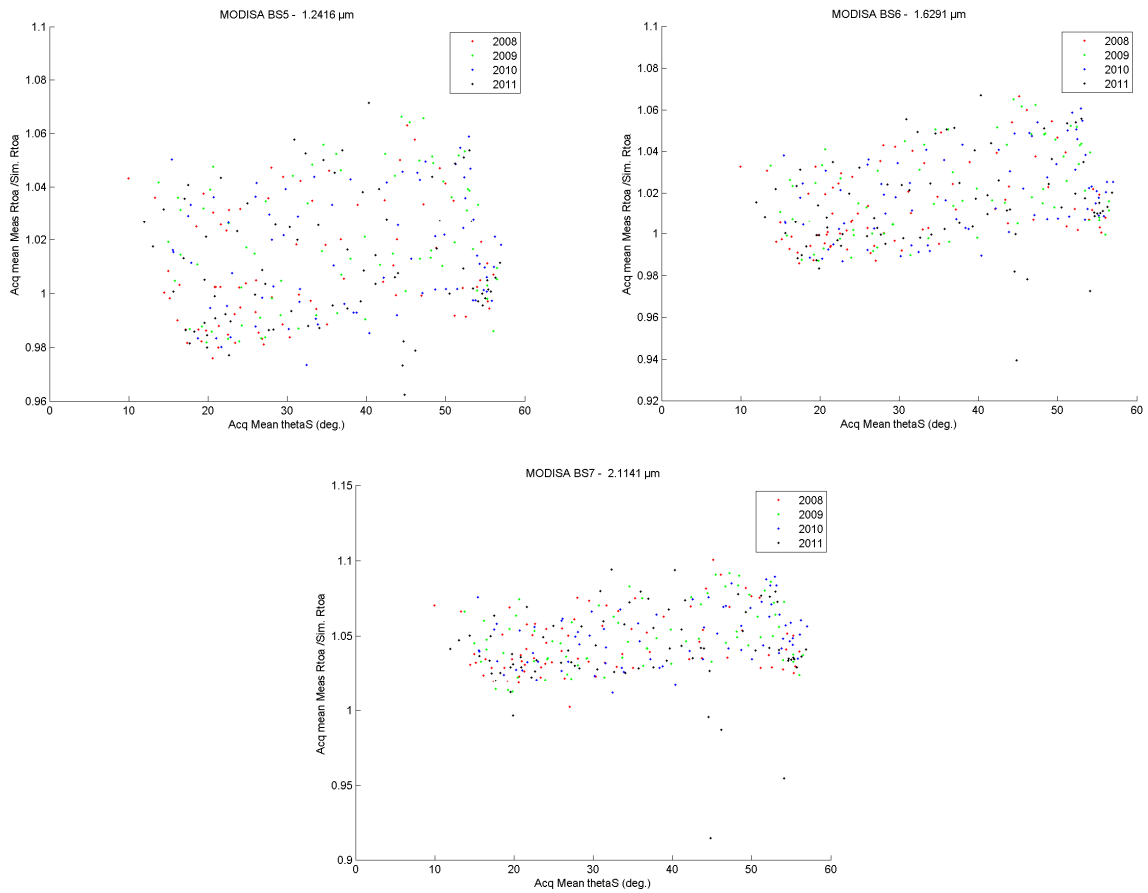


Figure 16: Temporal variability of the mean ratio of Measured to Simulated TOA reflectance versus Solar zenith Angle

4.2 Analysis of MERIS

4.2.1 Details of results for a single date

The following results and illustrations detail the estimation of the measured to simulated reflectance ratio for one date: MERIS acquisition of 31/07/2010. The illustration follows the implementation plan description in the previous section, step by step.

Read the database and select images



Figure 18: MERIS acquisition 31/07/2010 (Product MER_RR__1PRBCM20100731_085850_00000562091_00365_44006_0001_N1)

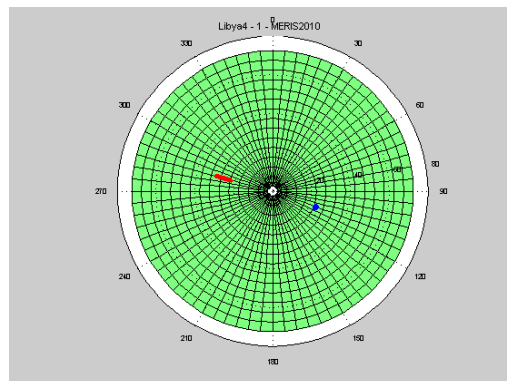


Figure 19: Polar diagram showing the geometry of the acquisition. Solar and satellite configuration angles are represented in blue and red respectively.

Read the TOA reflectances of clear pixels acquired into the site footprint for the selected date.

The TOA reflectances in the VIS and NIR channel (6 and 13) are represented below. This representation is shown in image coordinates (Column/Row).

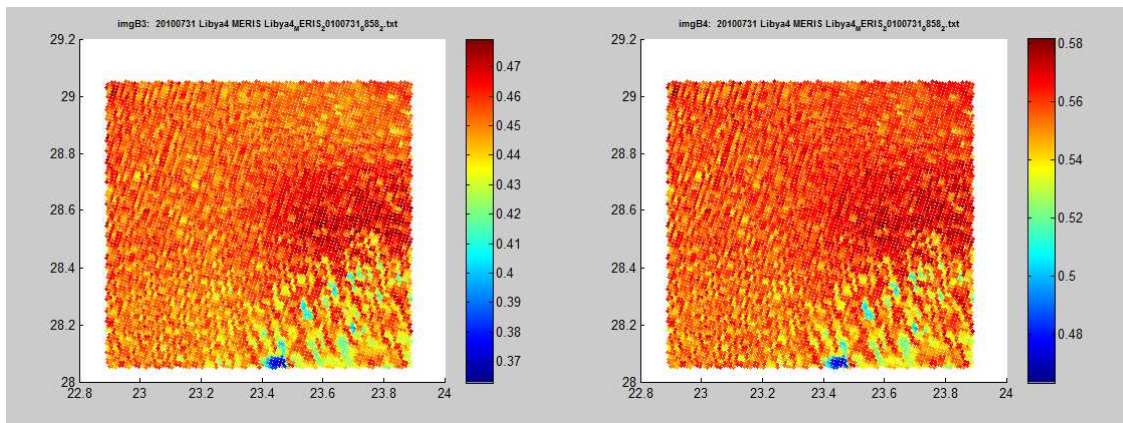


Figure 20: TOA reflectances in channels 6 (left) and 13 (right)

Check Pixels selection test

- Select valid pixels
- Select clear pixels
- Select scenes for which cloud coverage is less than 10%

A mask of valid pixel is applied is computed from the acquisition. These data are flagged inside the products, and the information is conserved in the data extracted from the ingestion module. The mask is represented hereafter.

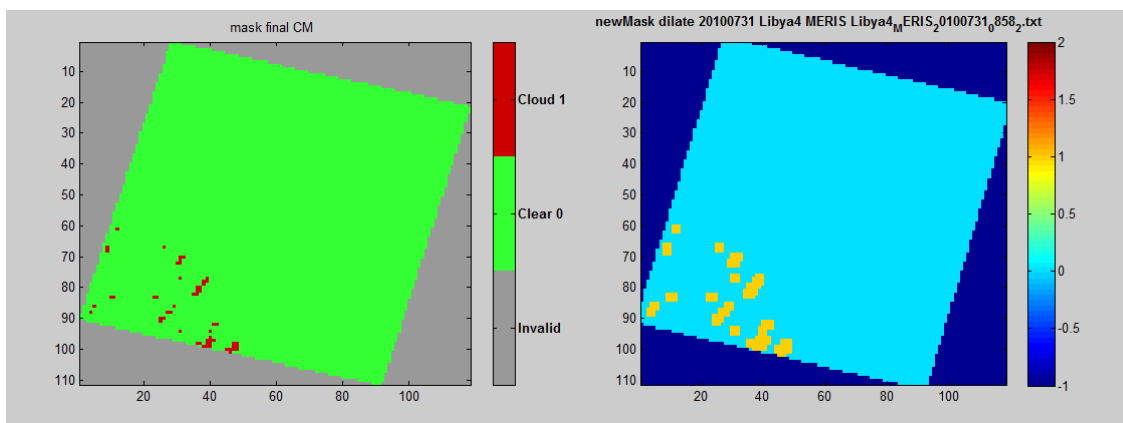


Figure 22: Cloud mask (left). Dilated cloud mask (right image)

Remarks: Cloud over-detection is highlighted in the area where the TOA reflectance is low (0.45). This will be corrected in the next version of the cloud detection.

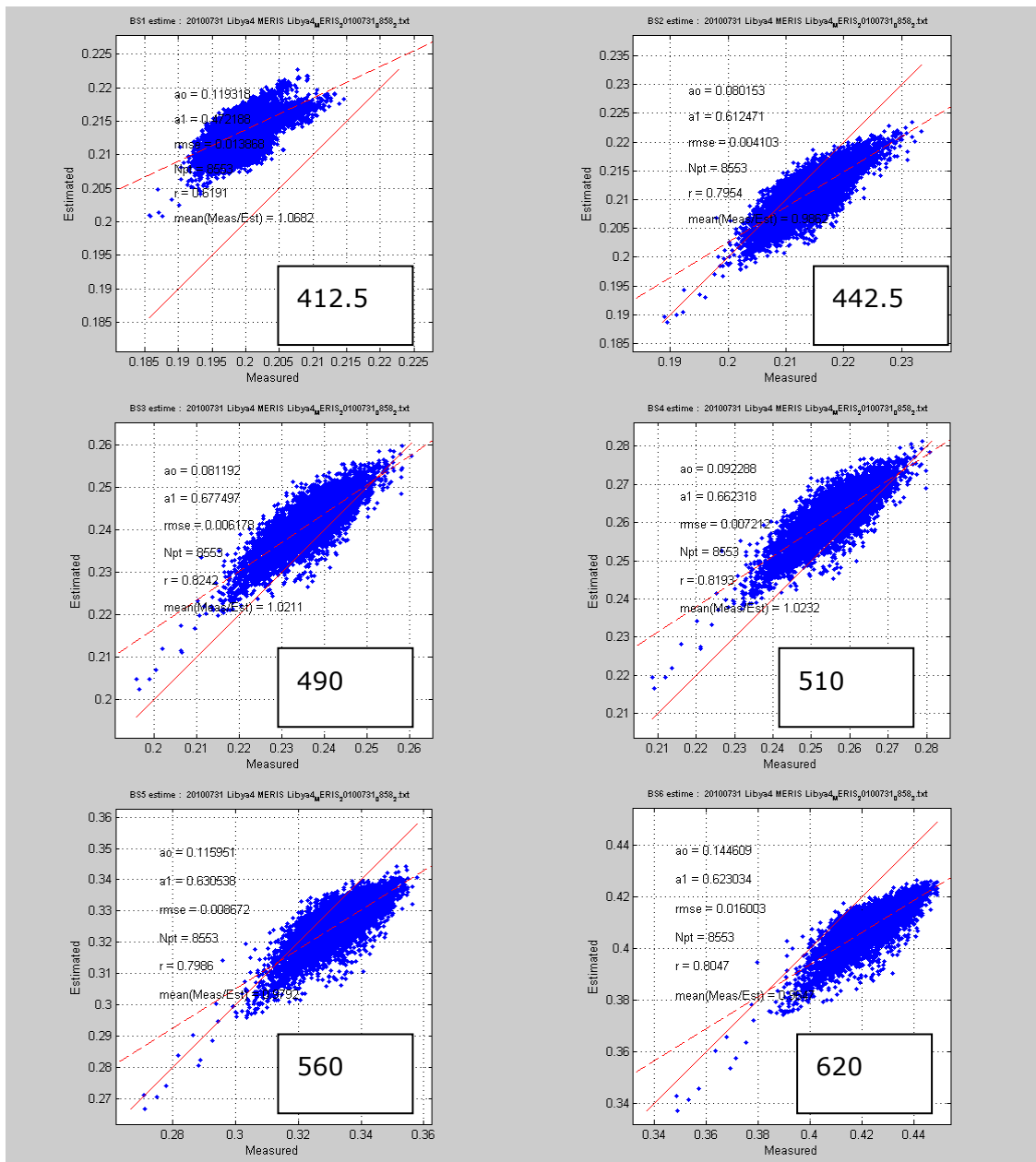
Correct TOA reflectances from gaseous absorption

The comparison of TOA measurements to the simulation is performed on TOA reflectance normalized to gaseous absorption.

The SMAC method allows to estimate the gaseous transmission for the atmospheric content read from ERA data at the date of acquisition. These coefficients are provided for each spectral bands used in the method.

Estimate the TOA reflectance in all MERIS bands using SMAC

The comparisons of the measurements versus the estimated TOA reflectance are shown in the next figures for all MERIS bands. Statistics of the regression are indicated inside the plots.



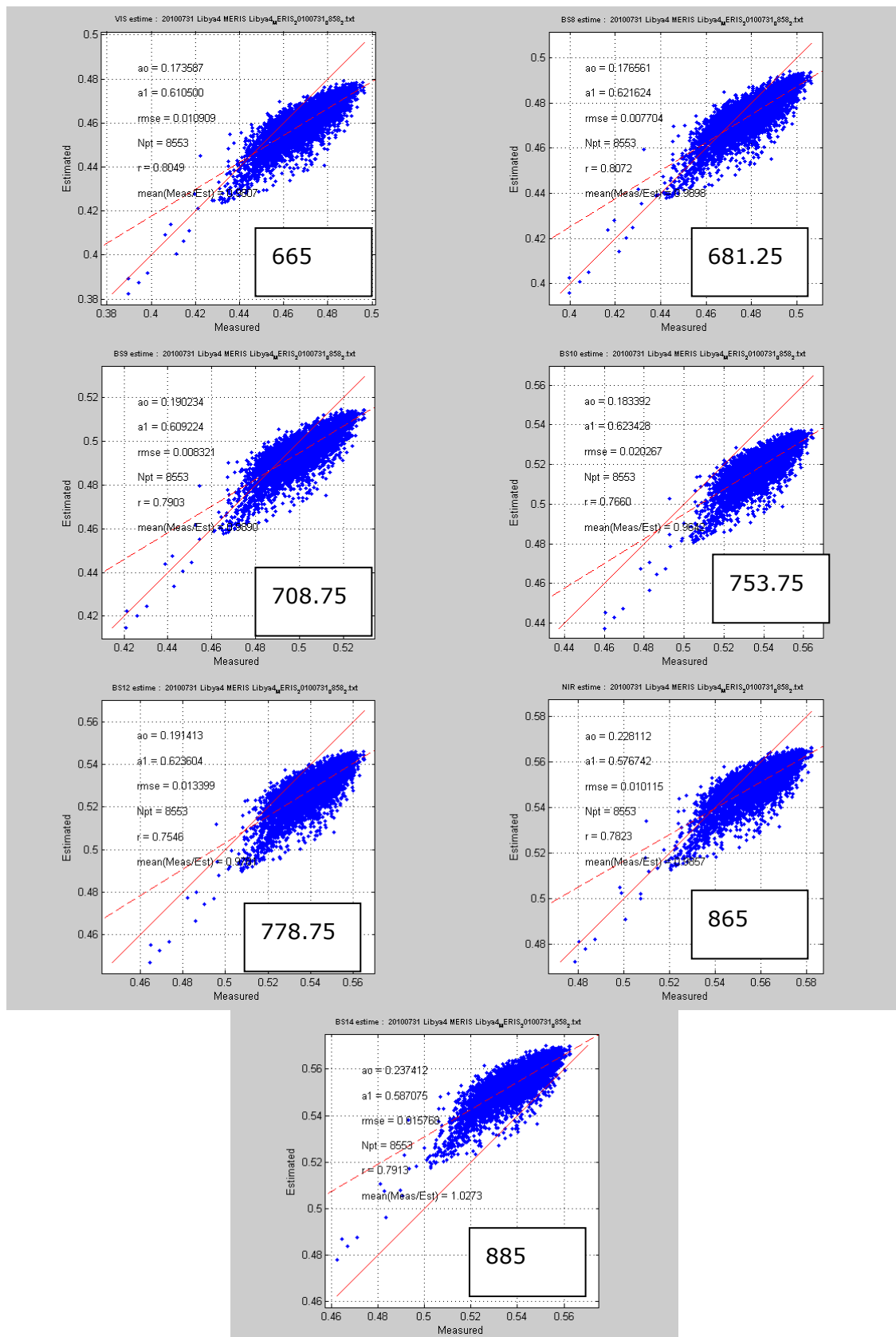


Figure 23: Scatterplot of simulated TOA reflectances versus measured TOA reflectances for 13 MERIS bands. Bands 11 and 15 are not simulated.

The spatial variability of the measured and simulated reflectances in the NIR channel is represented in the images below, together with the difference between the two maps. The highest difference is located in the top of the image.

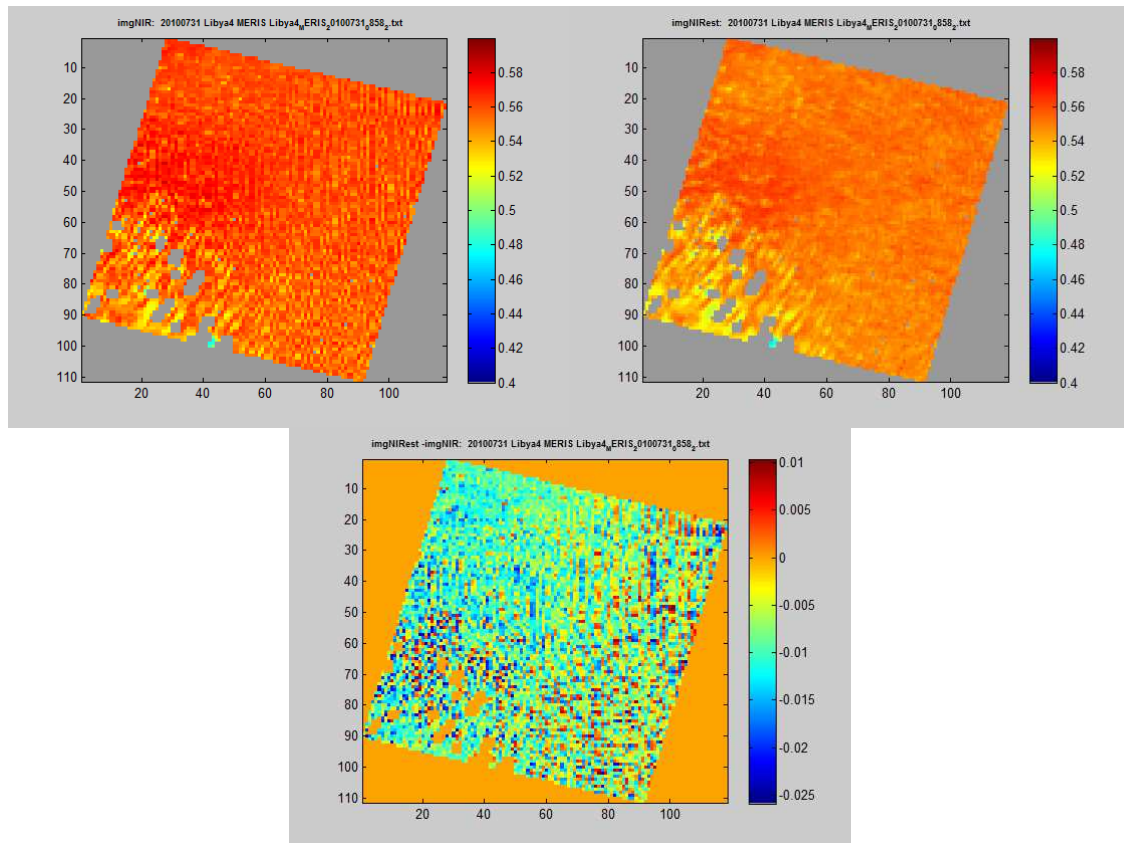


Figure 24: TOA reflectance in the NIR. Measured (top left), Simulated (top right), difference estimated minus measured (bottom).

Estimate the measured to simulated TOA reflectance ratio in the 13 MERIS bands

Once the simulated TOA reflectance estimated all the valid pixels, a map of the ratio is computed allowing to see the spatial variability and possible effects due to cloud edge. As an example, the map of reflectance ratio in the NIR channel is represented here after:

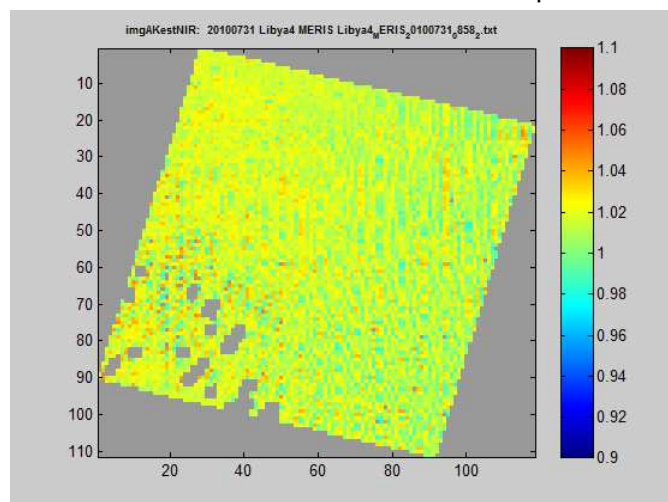


Figure 25: Map of reflectance ratio in the NIR band

The histograms of the reflectance ratio in the 13 bands are the following:

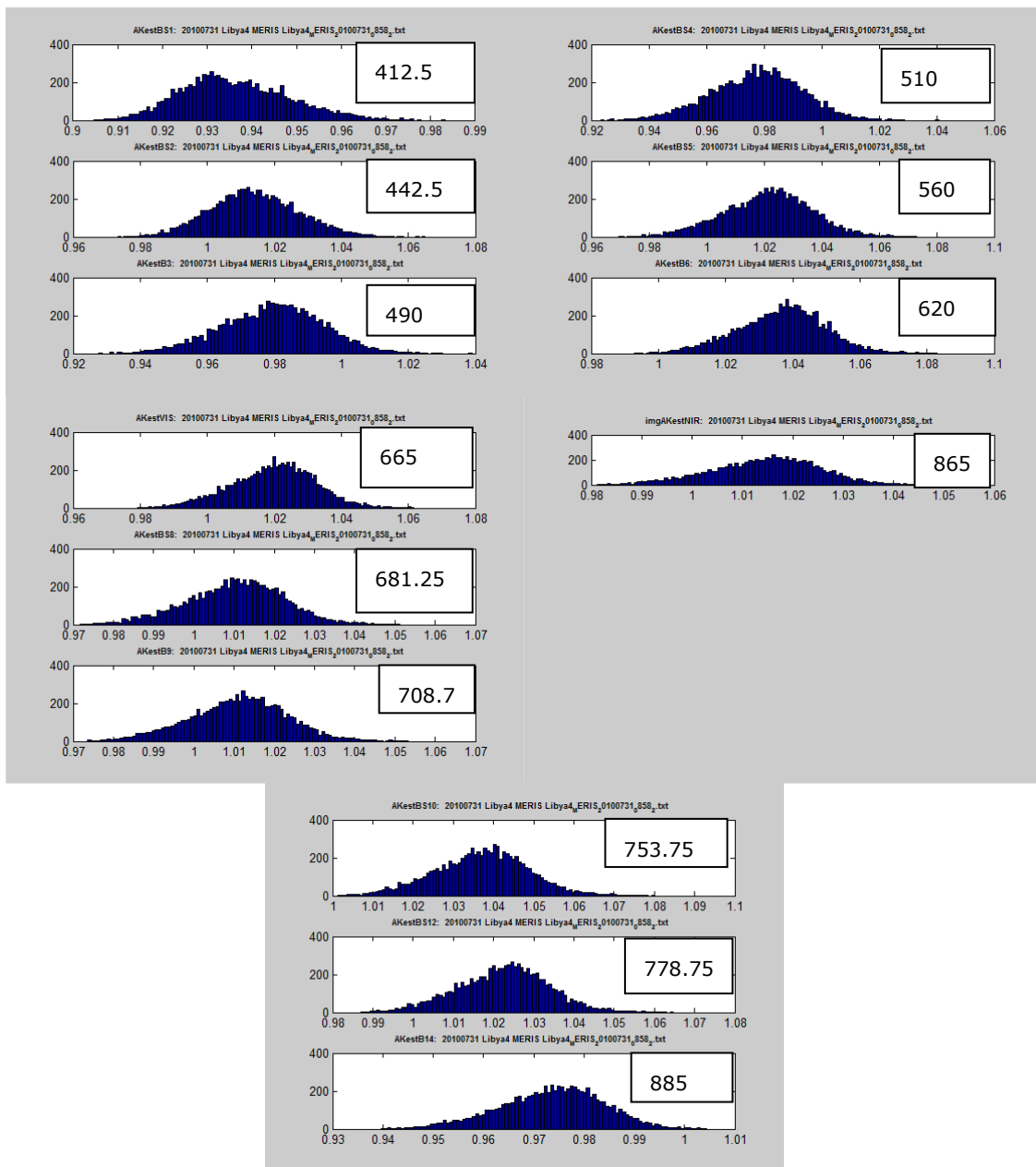
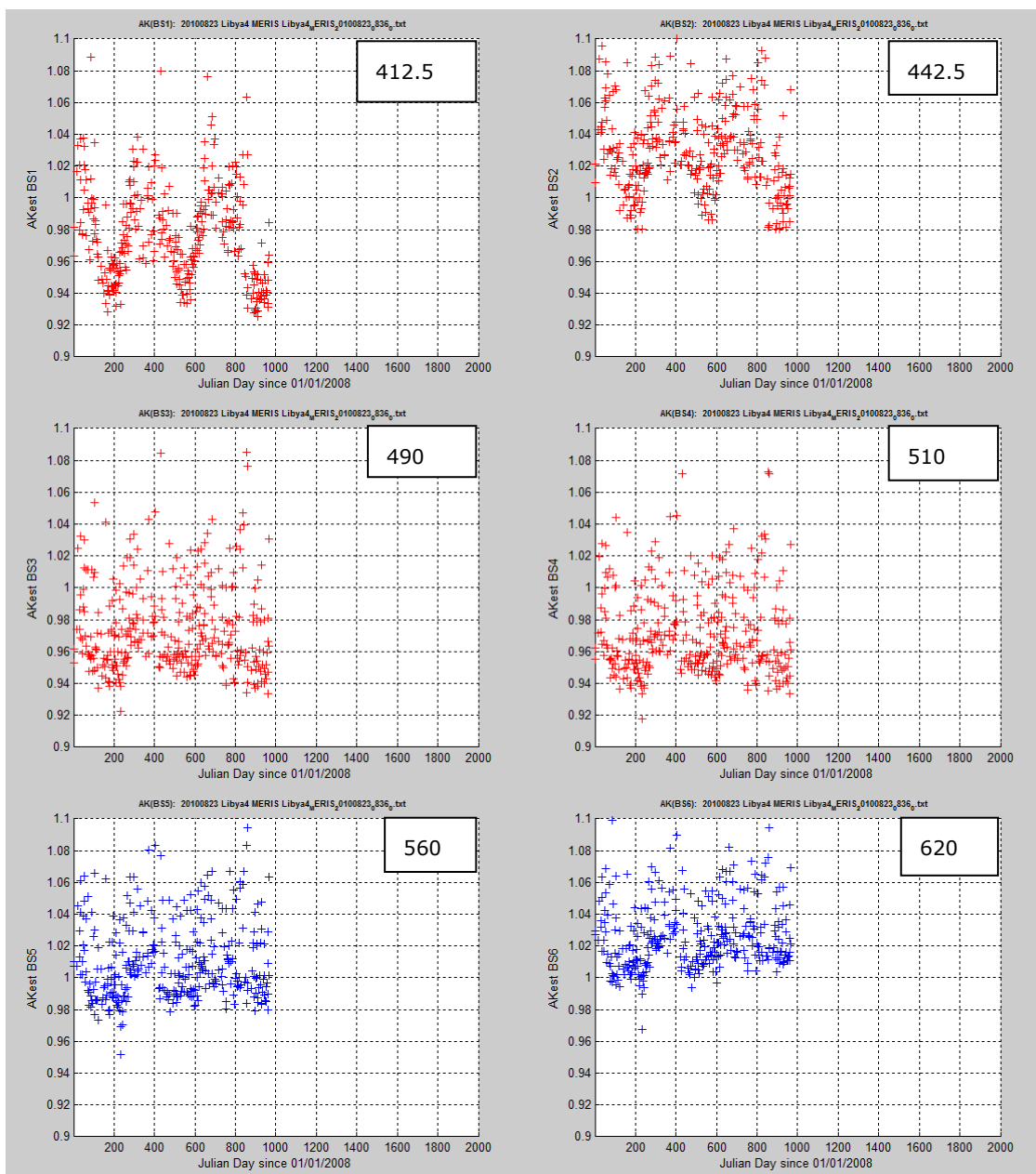


Figure 26: Ratio of Measured to Simulated TOA reflectance histograms

4.2.2 Multiyear results

The change in sensor radiometry is estimated by computing the mean of the measured to simulated TOA reflectances ratio for all available acquisitions. It is represented for the 13 bands in the figures below from 2008 to 2011.



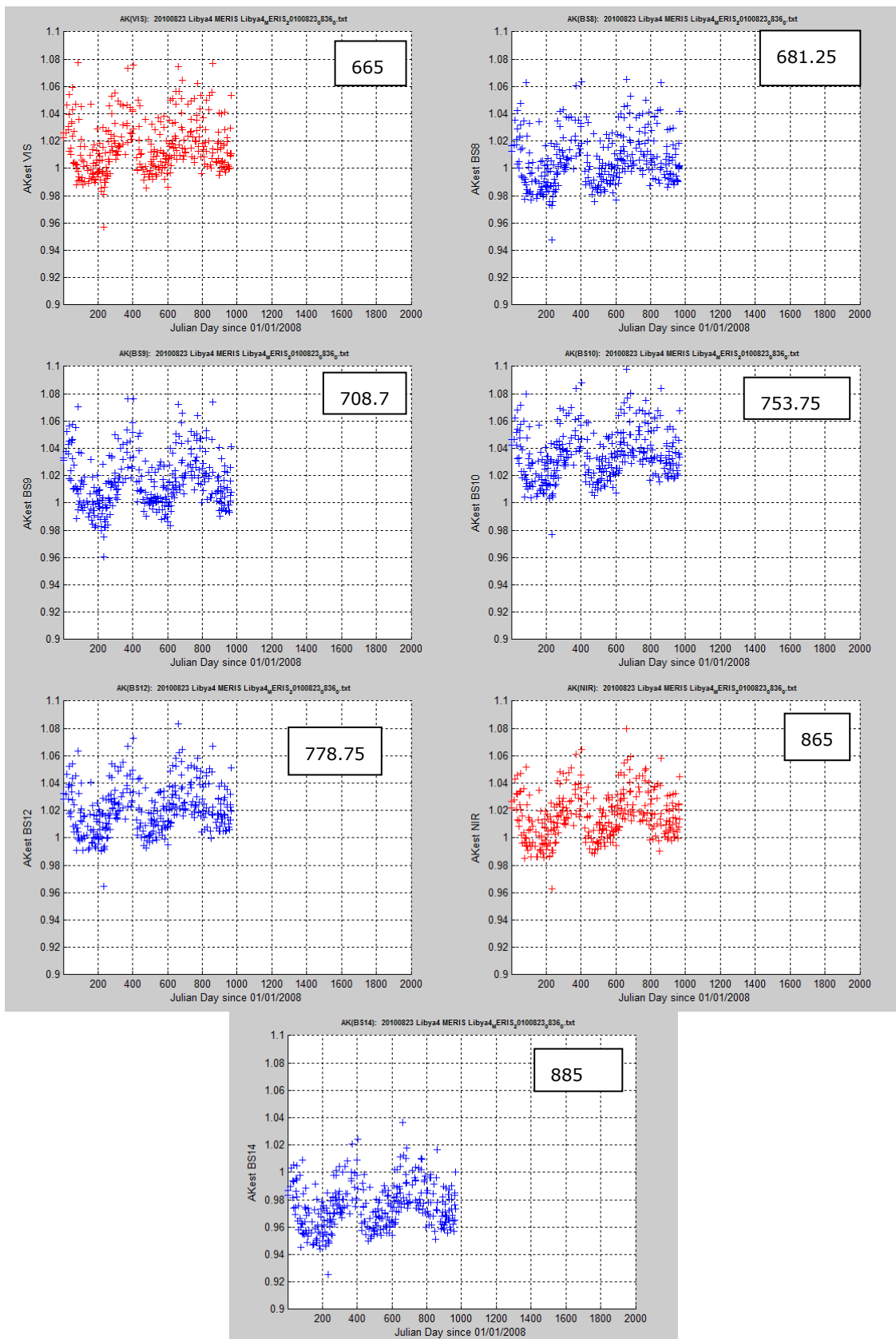


Figure 27: Temporal variability of the mean ratio between 2008 and 2011

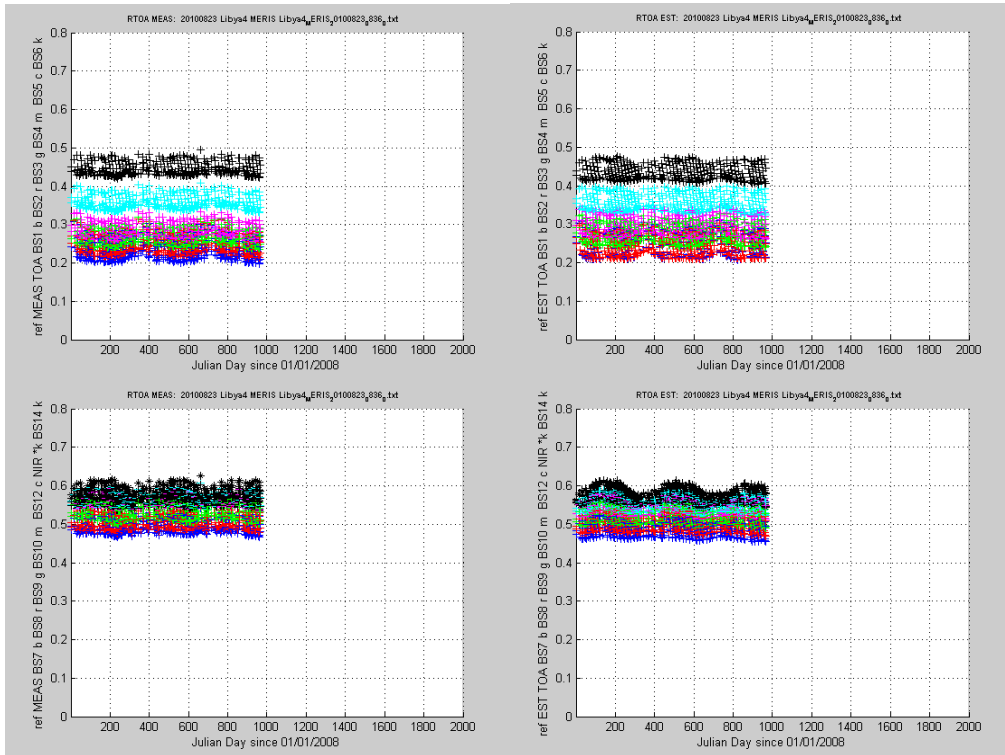


Figure 26: Temporal variability of the TOA reflectance (measured and simulated)

The variability of the ratio for four MERIS channels (ch.2, 5, 7 and 13) is plotted versus the mean solar zenith angle observed at the acquisition date.

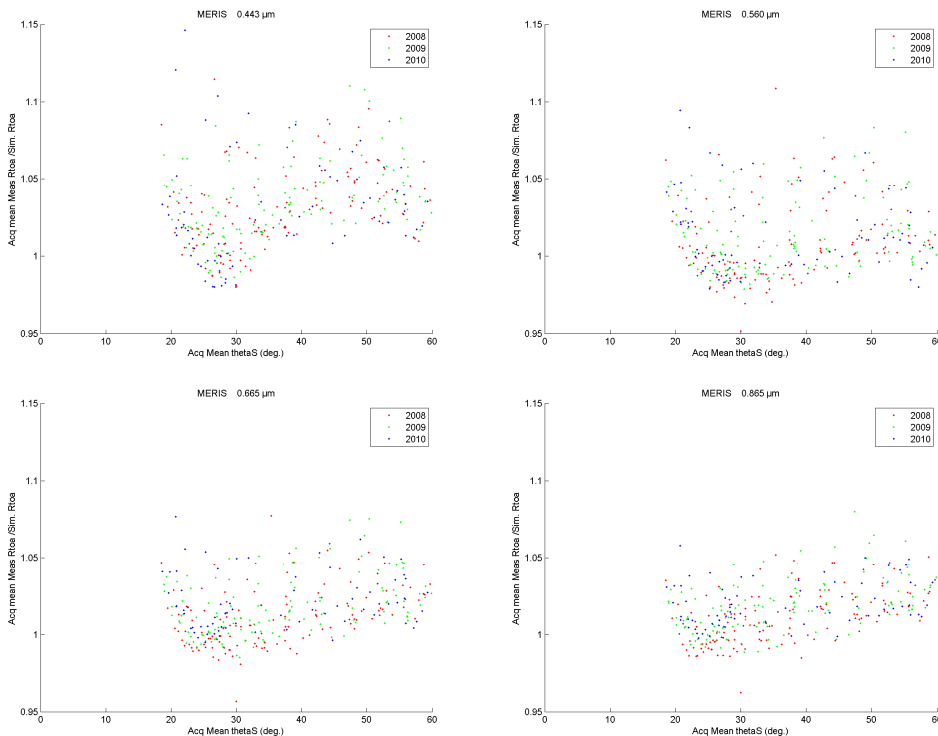


Figure 27: Temporal variability of the mean ratio of Measured to Simulated TOA reflectance versus Solar zenith Angle

4.3 Analysis of PARASOL

4.3.1 Details of results for a single date

The following results and illustrations detail the estimation of the measured to simulated reflectance ratio for one date: PARASOL acquisition of 04/08/2009. The illustration follows the implementation plan description in the previous section, step by step.

Results are relative to direction 1.

Read the database and select images

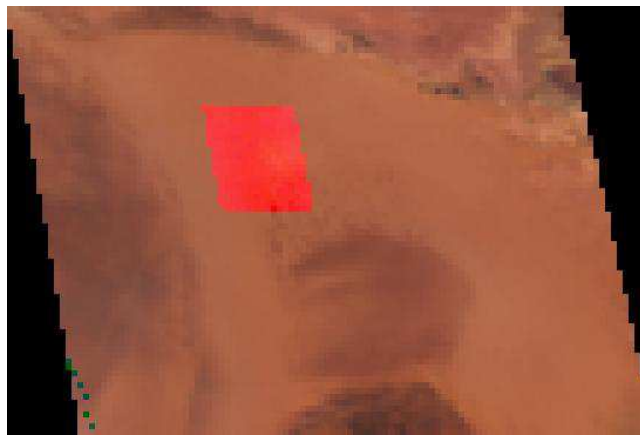


Figure 18: PARASOL acquisition 04/08/2009 (Product P3L1TBG1107109KD_n30_00_N26_00_e021_00_E027_00)

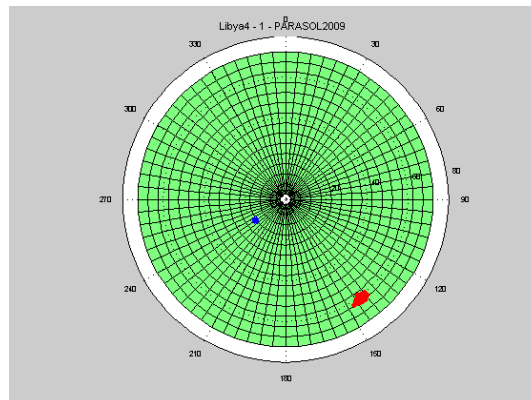


Figure 19: Polar diagram showing the geometry of the acquisition. Solar and satellite configuration angles are represented in blue and red respectively.

Read the TOA reflectances of clear pixels acquired into the site footprint for the selected date.

The TOA reflectances NIR channel (Band 7) is represented below. This representation is shown in image coordinates (Column/Row).

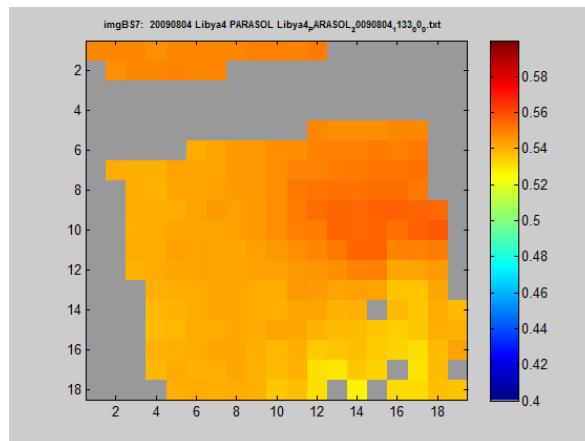


Figure 20: TOA reflectances in channel 7 (right)

Check Pixels selection test

- Select valid pixels
- Select clear pixels
- Select scenes for which cloud coverage is less than 10%

Correct TOA reflectances from gaseous absorption

The comparison of TOA measurements to the simulation is performed on TOA reflectance normalized to gaseous absorption.

The SMAC method allows to estimate the gaseous transmission for the atmospheric content read from ERA data at the date of acquisition. These coefficients are provided for each spectral bands used in the method.

Estimate the TOA reflectance in all MERIS bands using SMAC

The comparisons of the measurements versus the estimated TOA reflectance are shown in the next figures for all PARASOL bands. Statistics of the regression are indicated inside the plots.

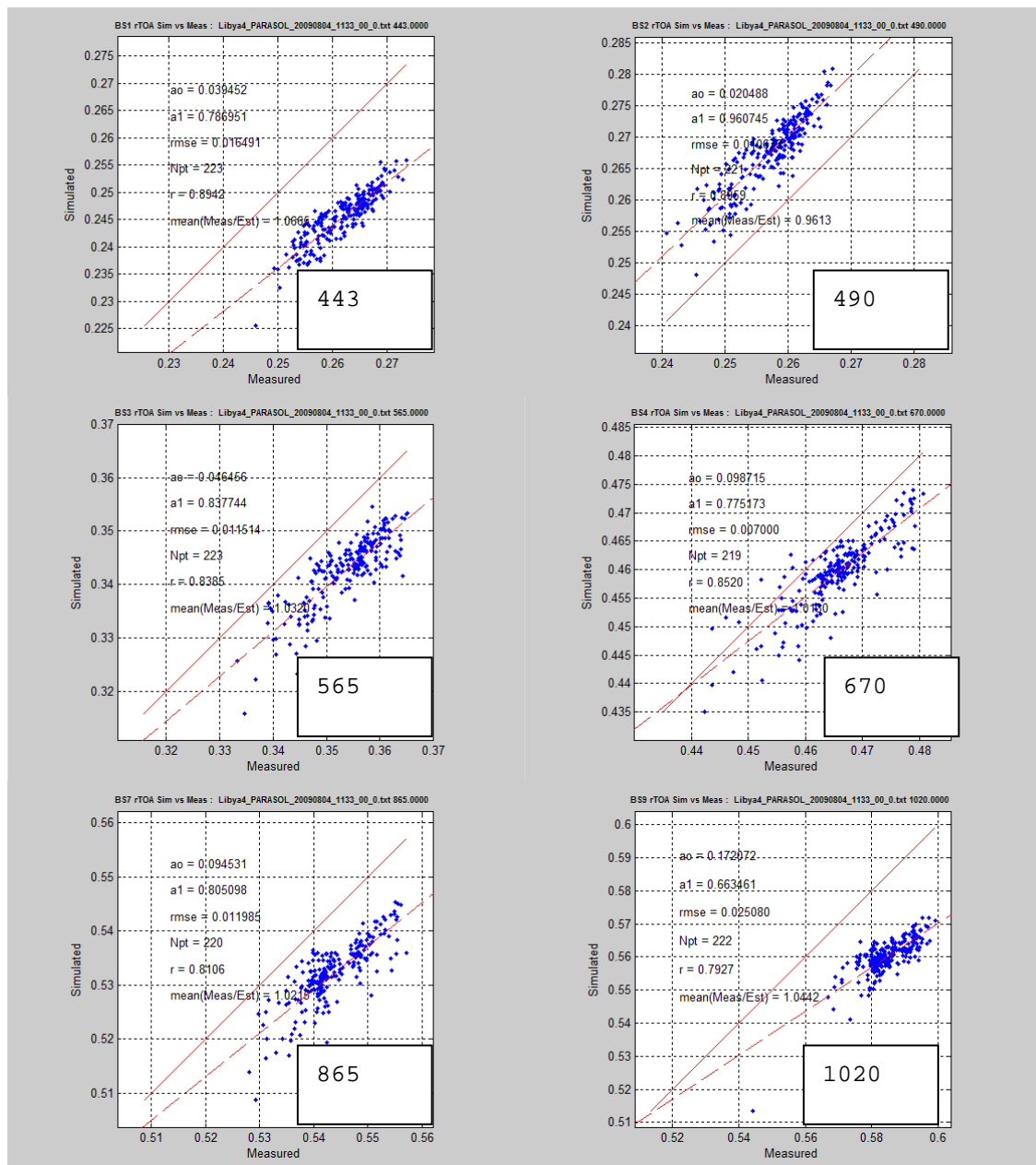


Figure 23: Scatterplot of simulated TOA reflectances versus measured TOA reflectances for 6 PARASOL bands. Bands 5, 6 and 8 are simulated.

The spatial variability of the measured and simulated reflectances in the NIR channel is represented in the images below, together with the difference between the two maps. The highest difference is located in the top of the image.

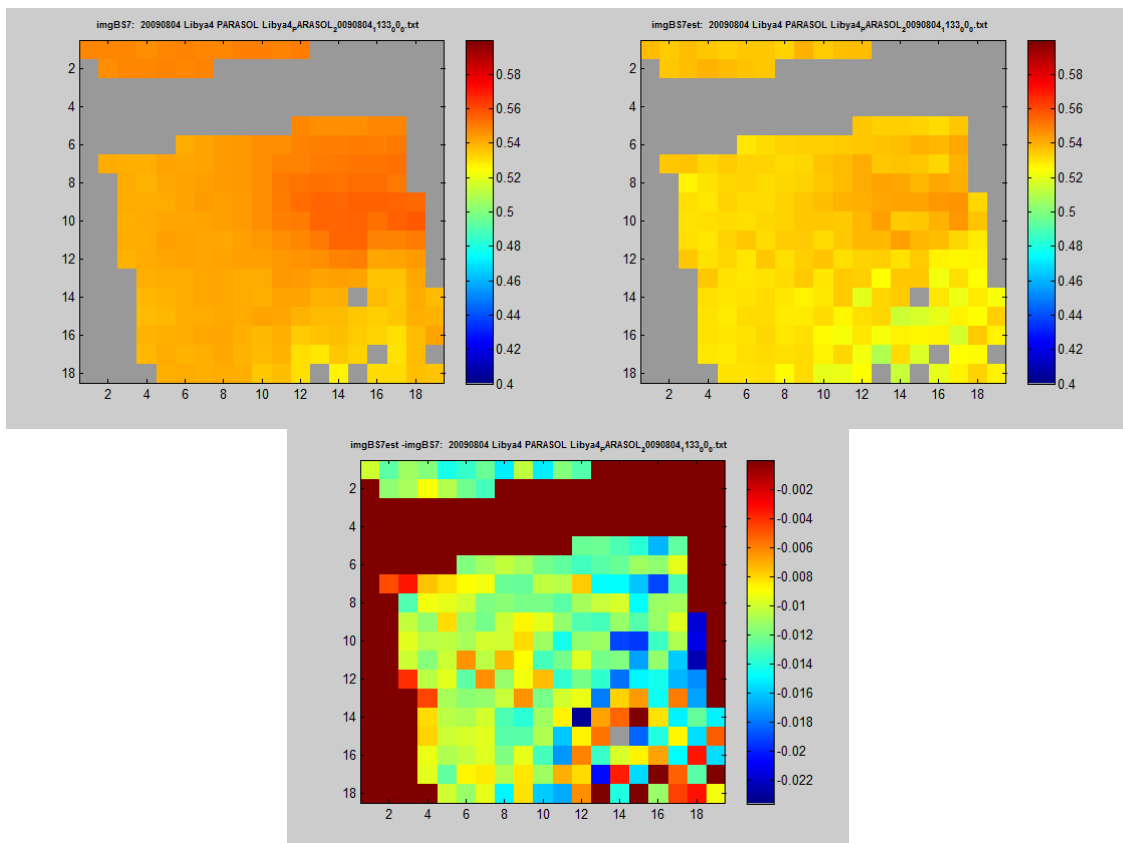


Figure 24: TOA reflectance in the NIR. Measured (top left), Simulated (top right), difference estimated minus measured (bottom).

Estimate the measured to simulated TOA reflectance ratio in the 13 MERIS bands

Once the simulated TOA reflectance estimated all the valid pixels, a map of the ratio is computed allowing to see the spatial variability and possible effects due to cloud edge. As an example, the map of reflectance ratio in the NIR channel is represented here after:

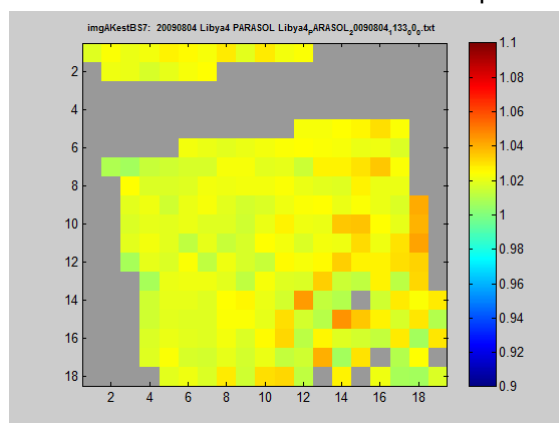


Figure 25: Map of reflectance ratio in the NIR band

The histograms of the reflectance ratio in the 13 bands are the following:

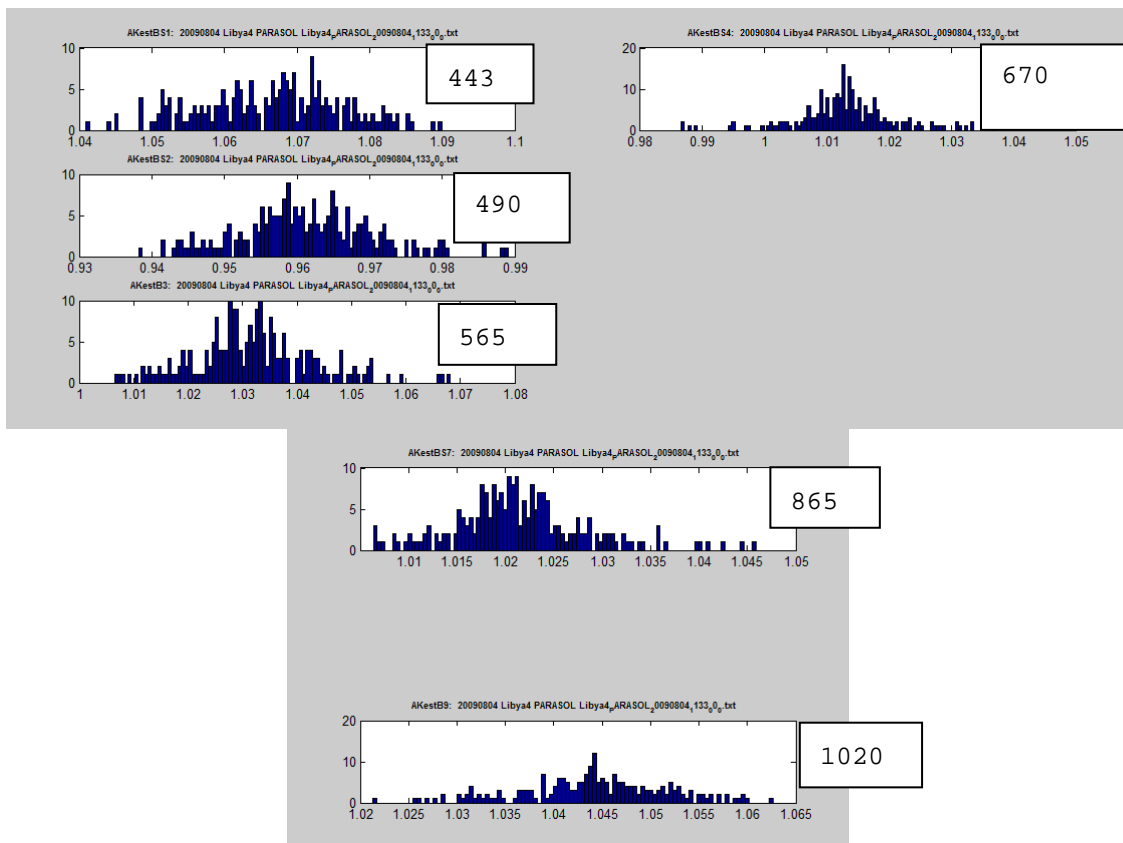


Figure 26: Ratio of Measured to Simulated TOA reflectance histograms

4.3.2 Multiyear results

The change in sensor radiometry is estimated by computing the mean of the measured to simulated TOA reflectances ratio for all available acquisitions. It is represented for the 13 bands in the figures below from 2008 to 2011.

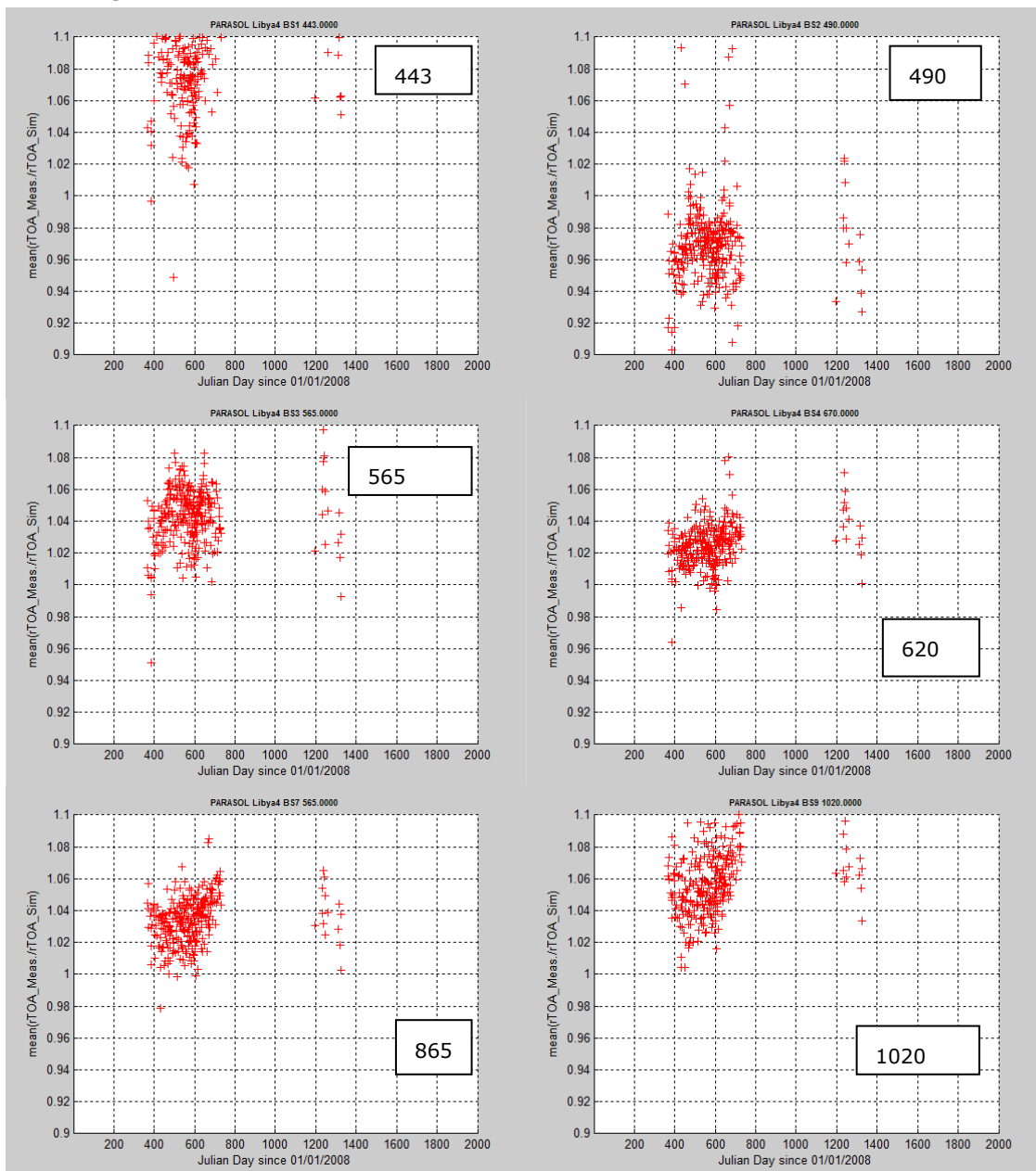


Figure 27: Temporal variability of the mean ratio between 2008 and 2011

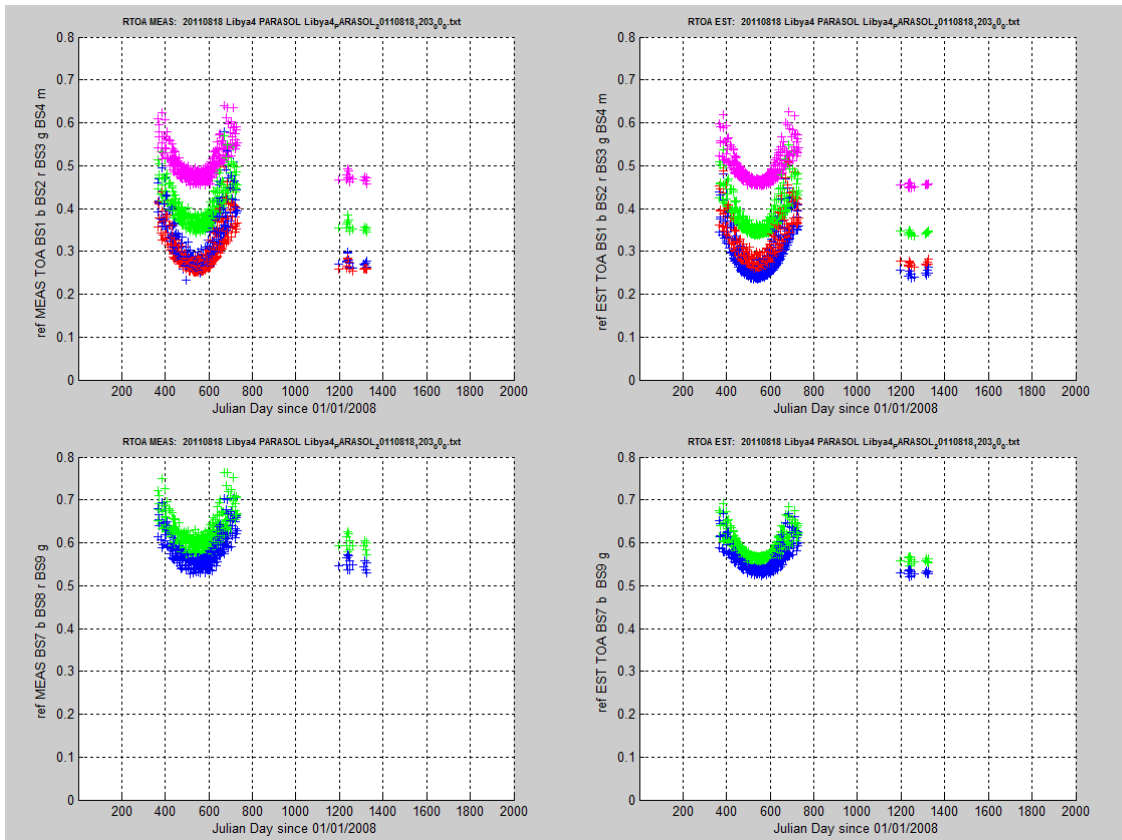


Figure 26: Temporal variability of the TOA reflectance (measured and simulated)

The variability of the ratio for NIR channels (Ch. 7) is plotted versus the mean solar zenith angle observed at the acquisition date.

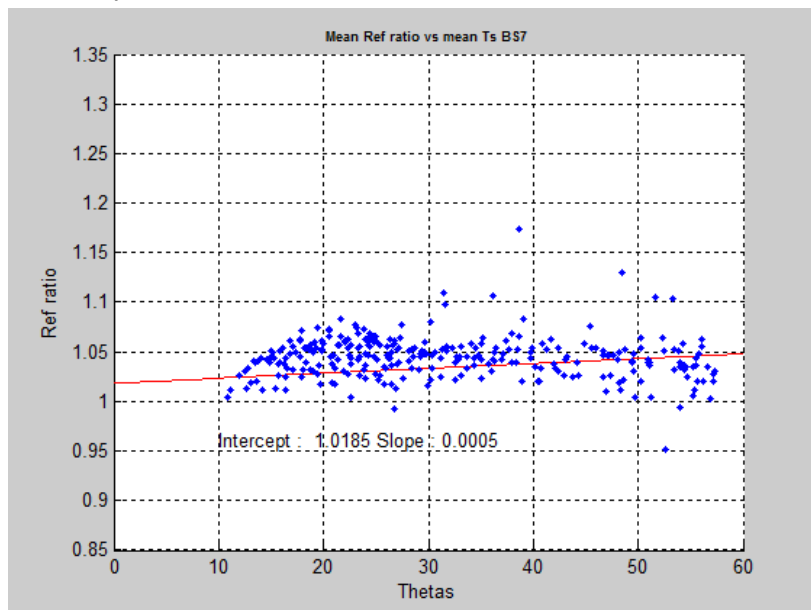


Figure 27: Temporal variability of the mean ratio of Measured to Simulated TOA reflectance versus Solar zenith Angle

4.4 Analysis of AASTR

4.4.1 Details of results for a single date

The following results and illustrations detail the estimation of the reflectance ratio for one date: AASTSR acquisition of 15/06/2008. The illustration follows the implementation plan description in the previous section, step by step.

Read the database and select images

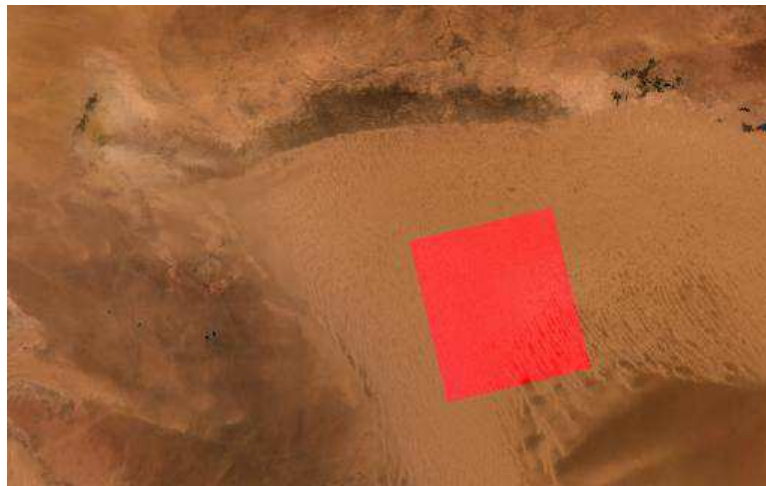


Figure 30: AASTSR acquisition 15/06/2008
(ATS_TOA_1PNMAP20080615_084739_00000482069_00279_32898_0001_N1)

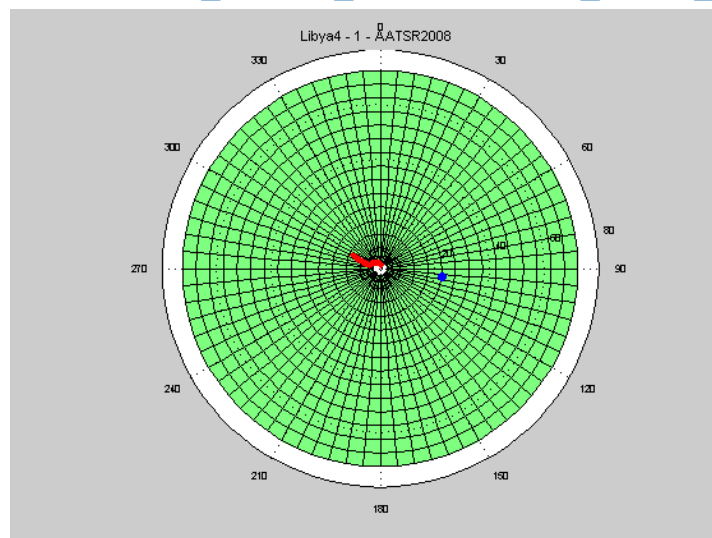


Figure 31: Polar diagram showing the geometry of the acquisition. Solar in blue, satellite in red.

Read the TOA reflectances of clear pixels acquired into the site footprint for the selected date.

The TOA reflectance the four AASTSR channels are represented below. This representation is shown in image coordinates (Column/Row).

Figure 32: TOA reflectances in B0, B2, B3 SWIR channels

Check Pixels selection test

- Select valid pixels
- Select clear pixels
- Select scenes for which cloud coverage is less than 10%

A mask of valid pixel is applied is computed from the acquisition. These data are flagged inside the products, and the information is conserved in the data extracted from the ingestion module. The mask is represented hereafter.

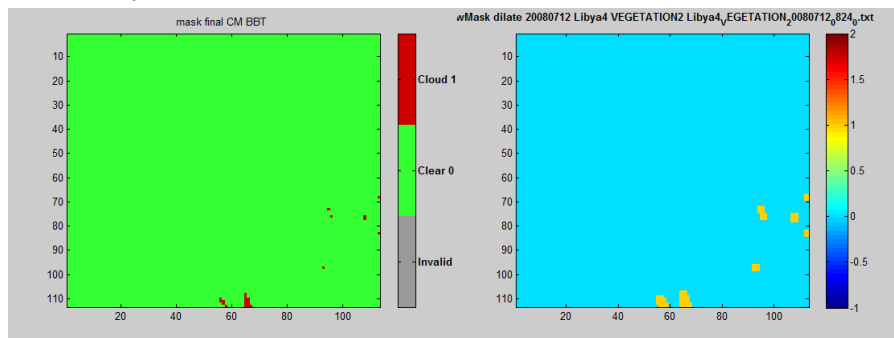


Figure 34: Cloud mask (left). Dilated cloud mask (right image)

Remarks: Cloud over-detection is highlighted in the area where the TOA reflectance is low (0.45). This will be corrected in the next version of the cloud detection.

Correct TOA reflectances from gaseous absorption

The comparison of TOA measurements to the simulation is performed on TOA reflectance normalized to gaseous absorption.

The SMAC method allows to estimate the gaseous transmission for the atmospheric content read from ERA data at the date of acquisition. These coefficients are provided for each spectral bands used in the method.

Estimate the TOA reflectance in the bands using SMAC

The comparisons of the measurements versus the estimated TOA reflectance are shown in the next figures for all AATSR bands. Statistics of the regression are indicated inside the plots.

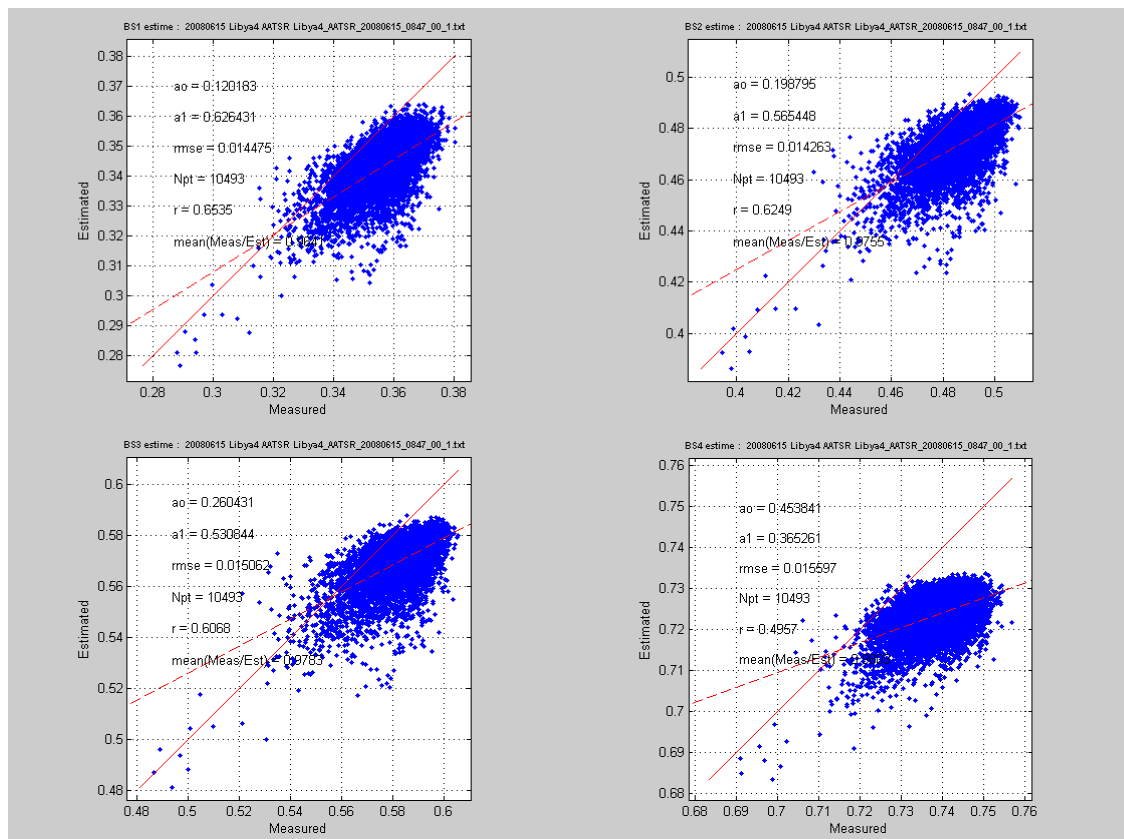


Figure 35: Scatterplot of simulated TOA reflectances versus measured TOA reflectances for all AATSR bands

The spatial variability of the measured and simulated reflectances in the NIR channel is represented in the images below, together with the difference between the two maps. The highest difference is located in the top of the image.

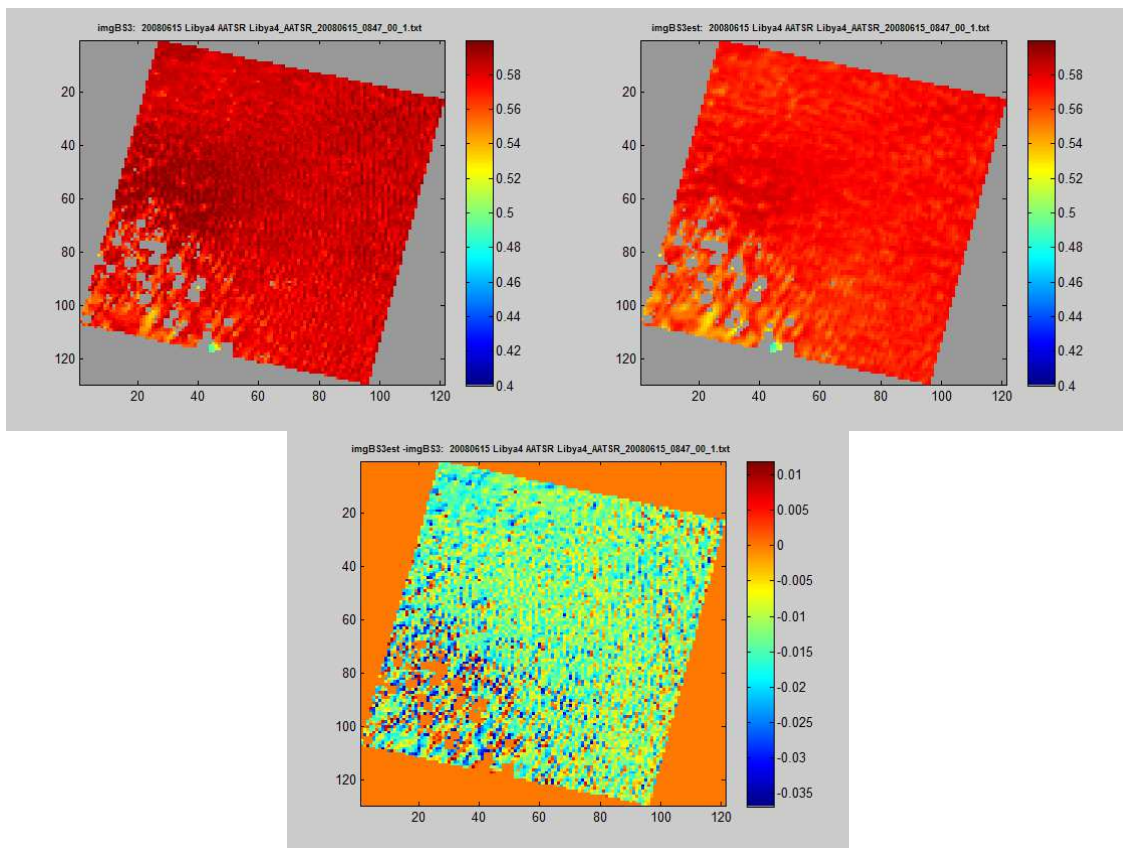


Figure 36: TOA reflectance in the NIR. Measured (top left), Simulated (top right), difference estimated minus measured (bottom).

Estimate the measured to simulated TOA reflectance ratio in the 4 VGT bands

Once the simulated TOA reflectance estimated all the valid pixels, a map of the ratio is computed allowing to see the spatial variability and possible effects due to cloud edge. As an example, the map of reflectance ratio in the NIR channel is represented here after:

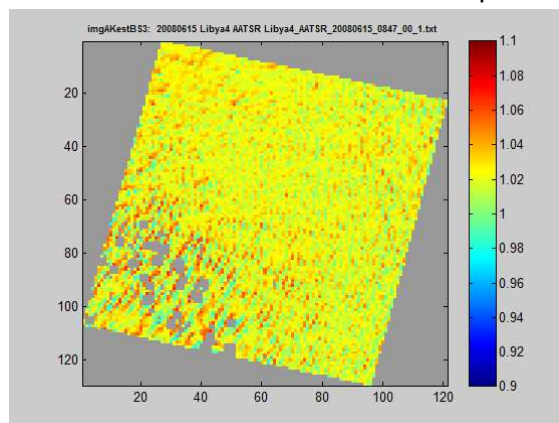


Figure 38: Map of reflectance ratio in the NIR band

The histograms of the reflectance ratio in the 4 bands are the following:

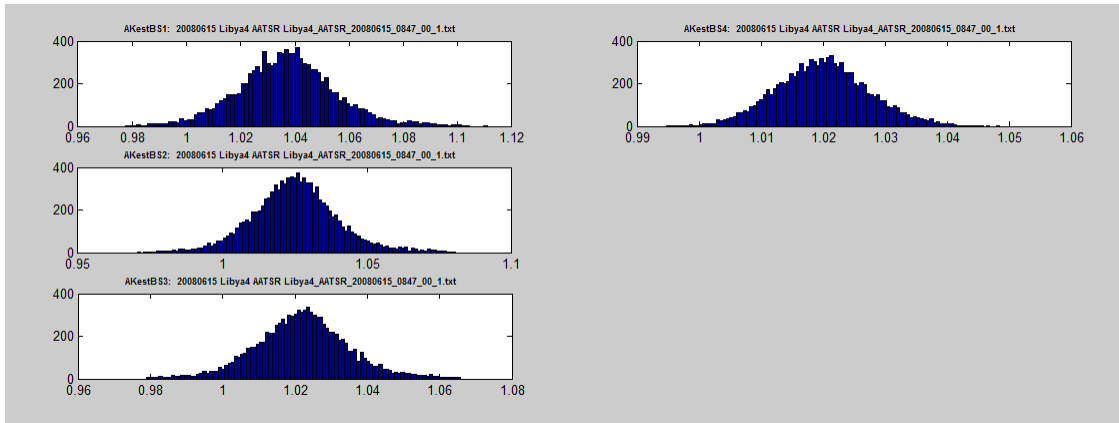


Figure 37: Ratio of Measured to Simulated TOA reflectance histograms

4.4.2 Multiyear results

The change in sensor radiometry is estimated by computing the mean of the measured to simulated TOA reflectances ratio for all available acquisitions. It is represented for the 4 bands in the figures below from 2008 to 2011.

4.4.2.1 Results related to nadir view

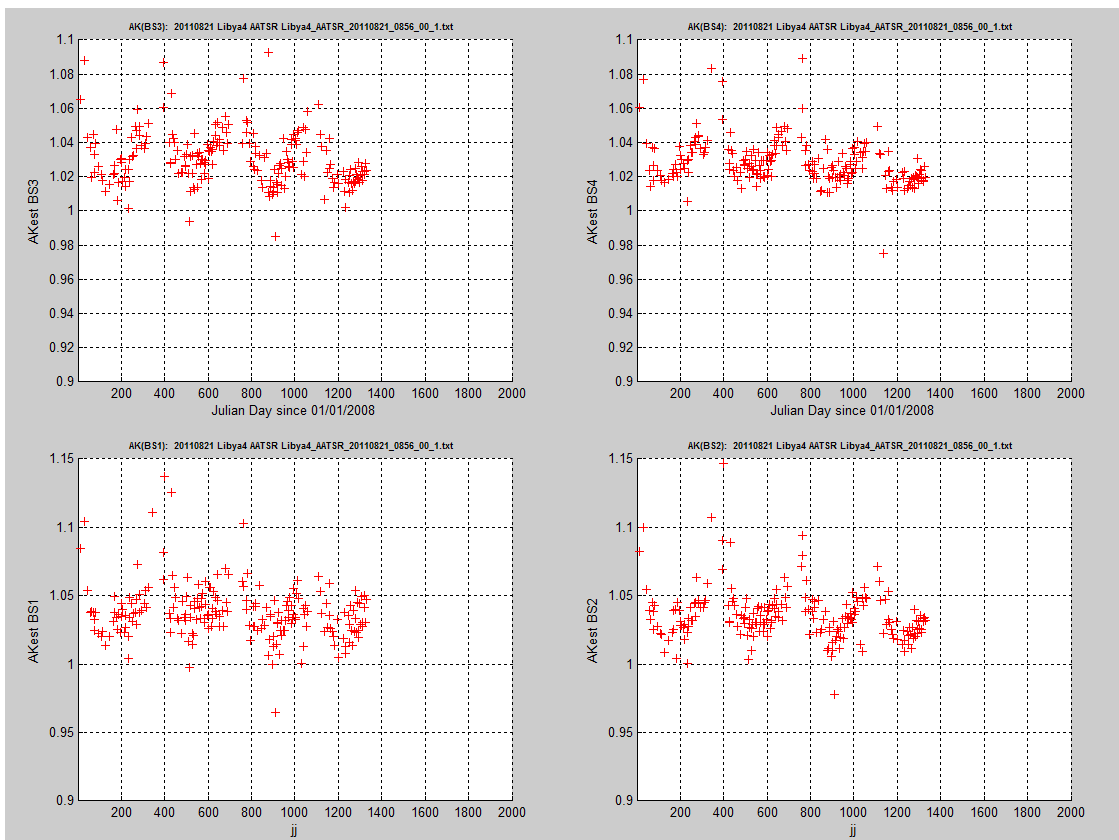


Figure 39: Temporal variability of the mean ratio between 2008 and 2011

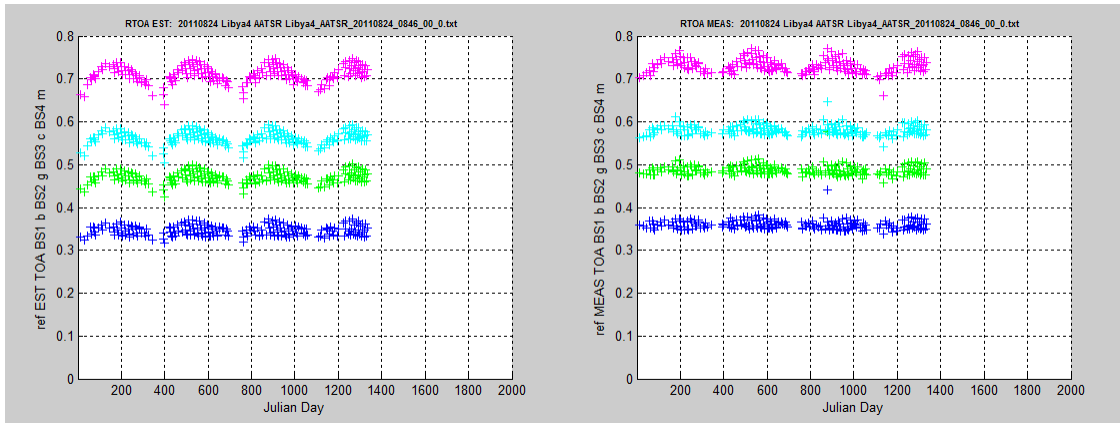


Figure 40: Temporal variability of the TOA reflectance (measured and simulated)

The variability of the ratio for four AATSR channels is plotted versus the mean solar zenith angle observed at the acquisition date.

Figure 27: Temporal variability of the mean ratio of Measured to Simulated TOA reflectance versus Solar zenith Angle

4.4.2.1 Results related to forward view

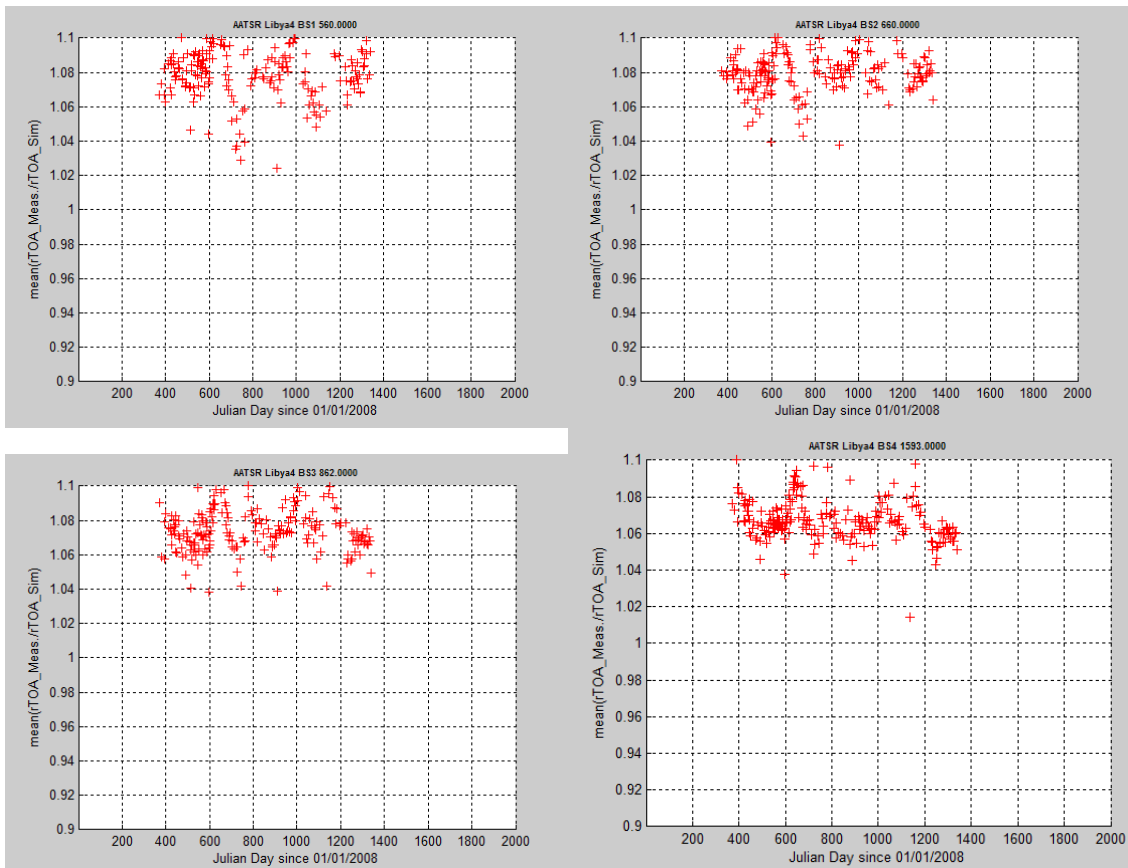


Figure 39: Temporal variability of the mean ratio between 2008 and 2011

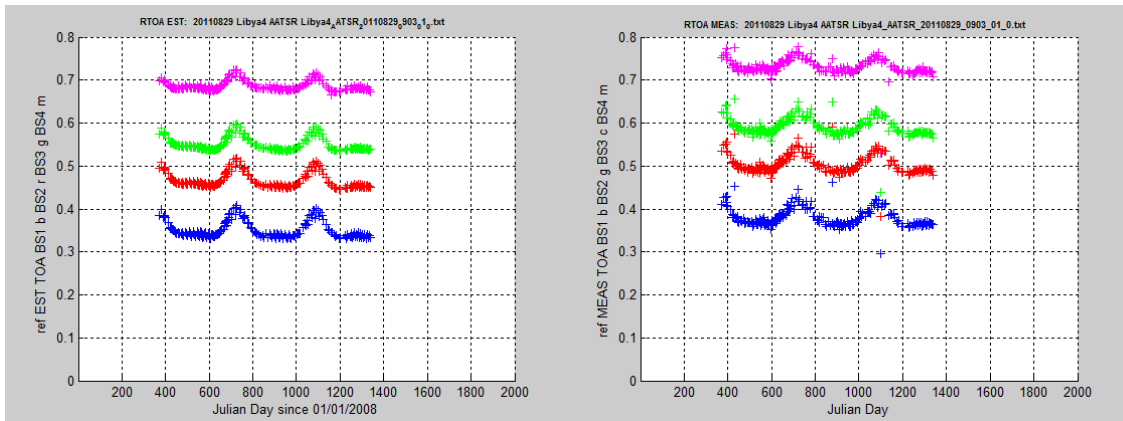


Figure 40: Temporal variability of the TOA reflectance (measured and simulated)

4.5 Analysis of VEGETATION

4.5.1 Details of results for a single date

The following results and illustrations detail the estimation of the reflectance ratio for one date: VEGETATION acquisition of 12/07/2008. The illustration follows the implementation plan description in the previous section, step by step.

Read the database and select images

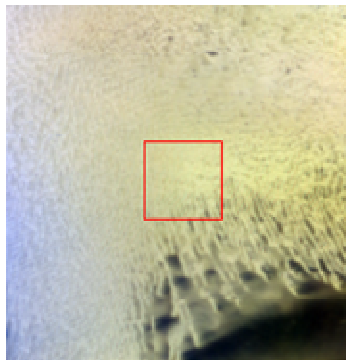


Figure 30: VEGETATION acquisition 31/07/2010 (V2KRNPL____20080712F026)

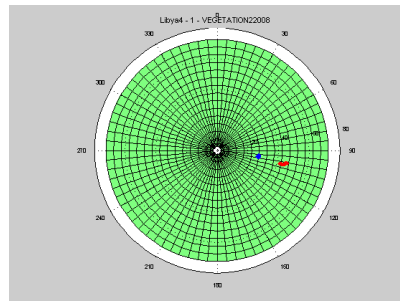


Figure 31: Polar diagram showing the geometry of the acquisition. Solar in blue, satellite in red.

Read the TOA reflectances of clear pixels acquired into the site footprint for the selected date.

The TOA reflectance the four VEGETATION channels are represented below. This representation is shown in image coordinates (Column/Row).

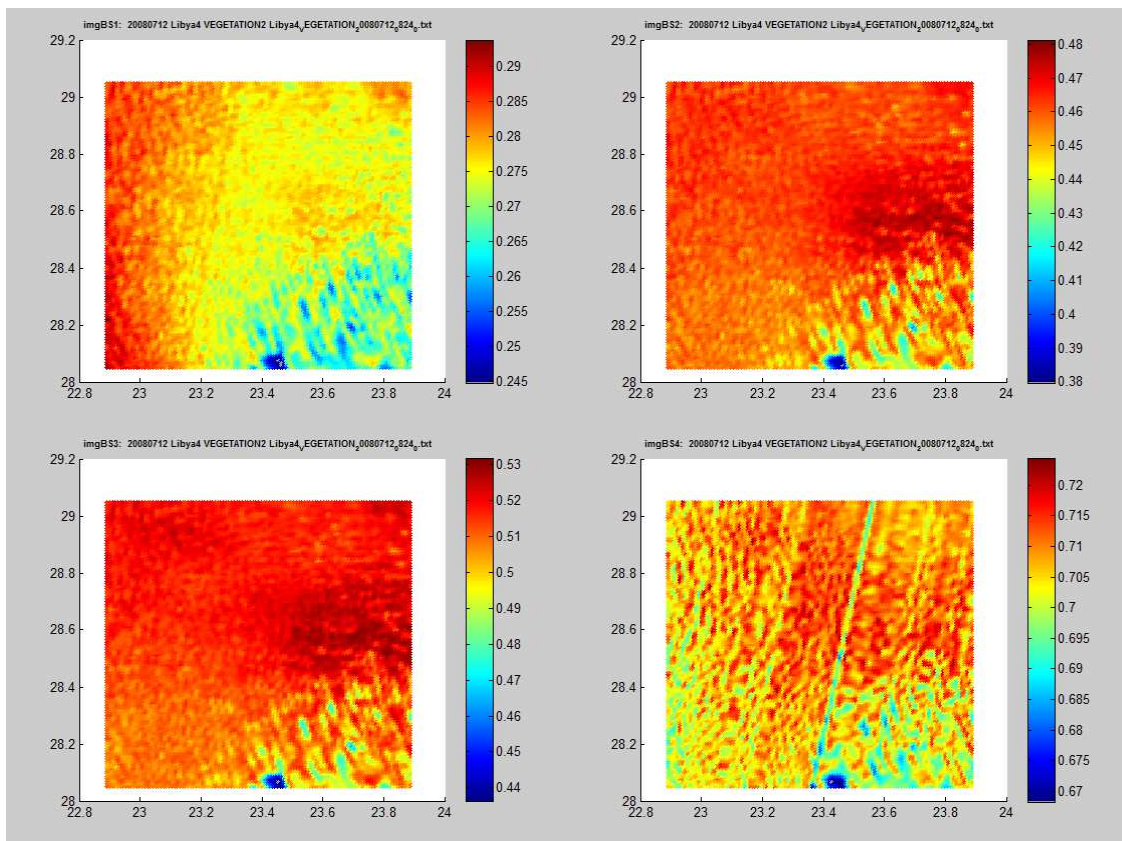


Figure 32: TOA reflectances in B0, B2, B3 SWIR channels

Check Pixels selection test

- Select valid pixels
- Select clear pixels
- Select scenes for which cloud coverage is less than 10%

A mask of valid pixel is applied is computed from the acquisition. These data are flagged inside the products, and the information is conserved in the data extracted from the ingestion module. The mask is represented hereafter.

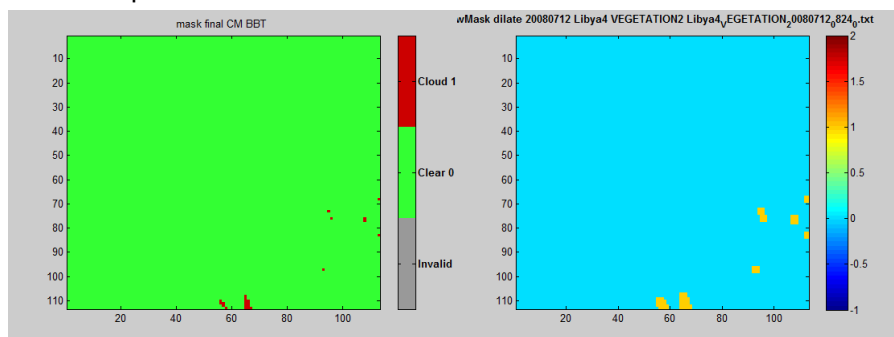


Figure 34: Cloud mask (left). Dilated cloud mask (right image)

Remarks: Cloud over-detection is highlighted in the area where the TOA reflectance is low (0.45). This will be corrected in the next version of the cloud detection.

Correct TOA reflectances from gaseous absorption

The comparison of TOA measurements to the simulation is performed on TOA reflectance normalized to gaseous absorption.

The SMAC method allows to estimate the gaseous transmission for the atmospheric content read from ERA data at the date of acquisition. These coefficients are provided for each spectral bands used in the method.

Estimate the TOA reflectance in the bands using SMAC

The comparisons of the measurements versus the estimated TOA reflectance are shown in the next figures for all VEGETATION bands. Statistics of the regression are indicated inside the plots.

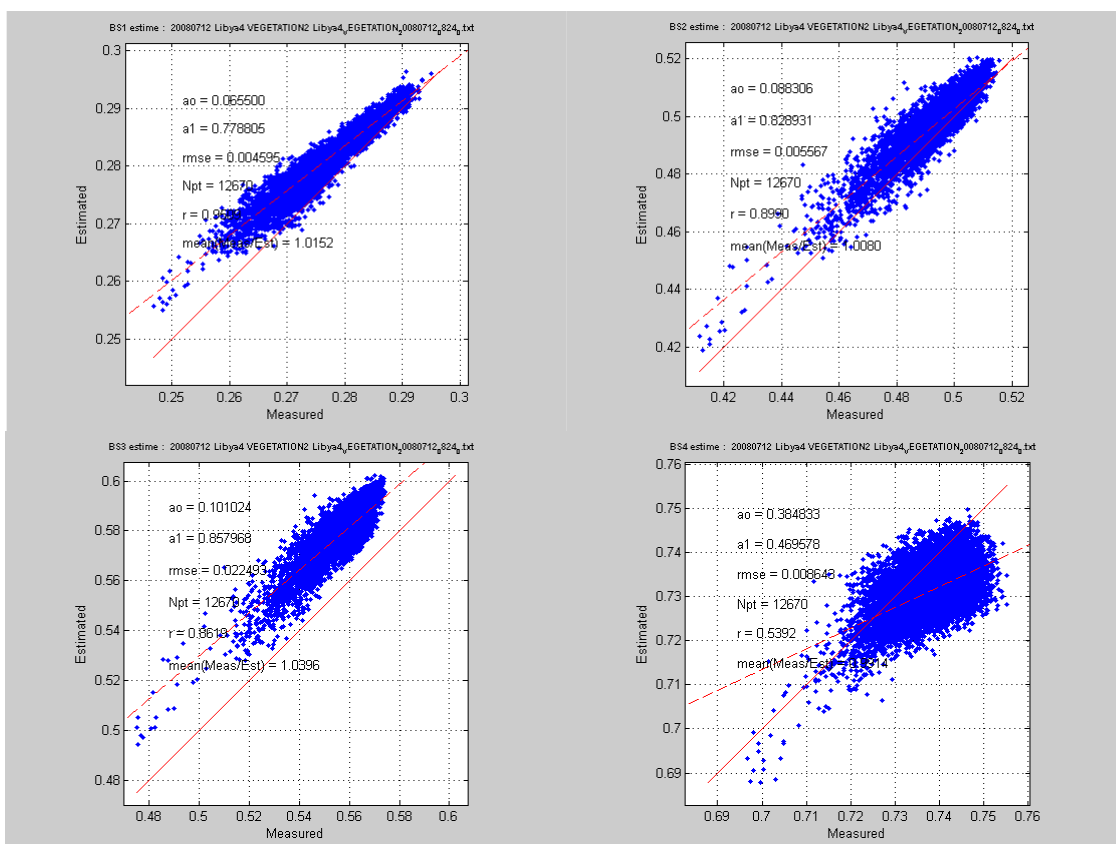


Figure 35: Scatterplot of simulated TOA reflectances versus measured TOA reflectances for all VEGETATION bands

The spatial variability of the measured and simulated reflectances in the NIR channel is represented in the images below, together with the difference between the two maps. The highest difference is located in the top of the image.

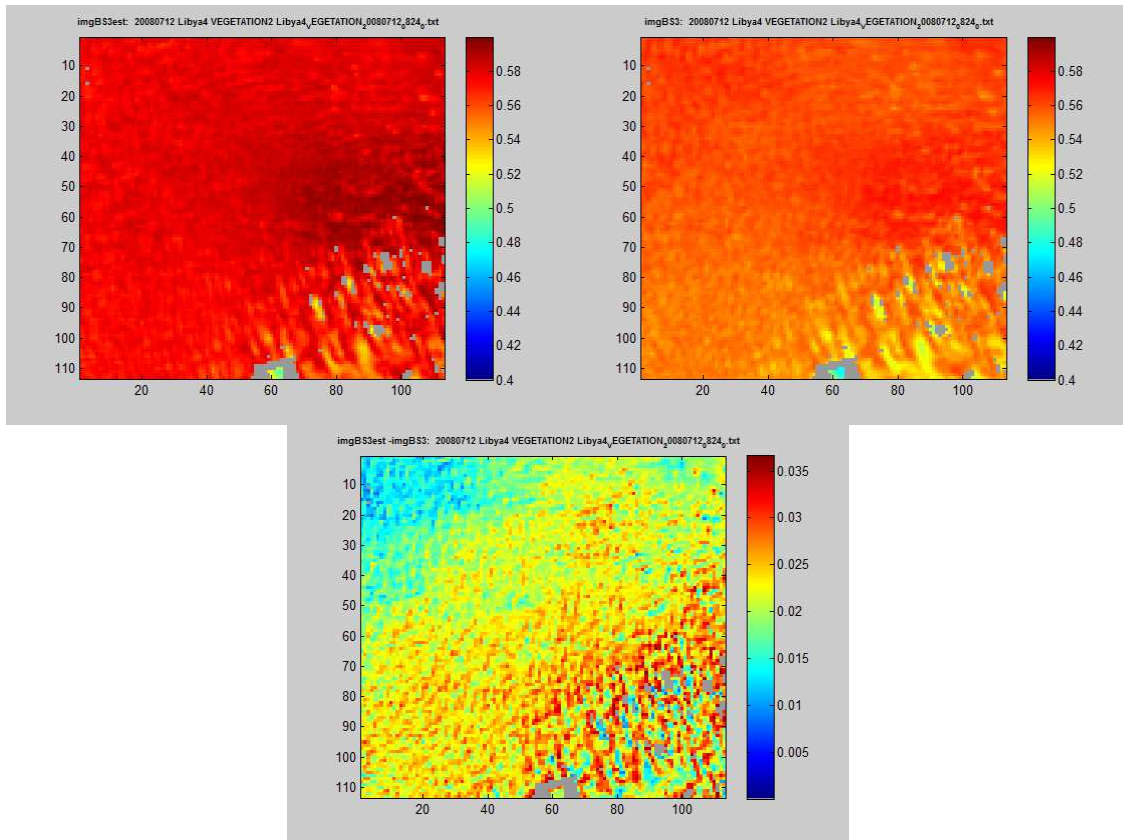


Figure 36: TOA reflectance in the NIR. Measured (top left), Simulated (top right), difference estimated minus measured (bottom).

Estimate the measured to simulated TOA reflectance ratio in the 4 VGT bands

Once the simulated TOA reflectance estimated all the valid pixels, a map of the ratio is computed allowing to see the spatial variability and possible effects due to cloud edge. As an example, the map of reflectance ratio in the NIR channel is represented here after:

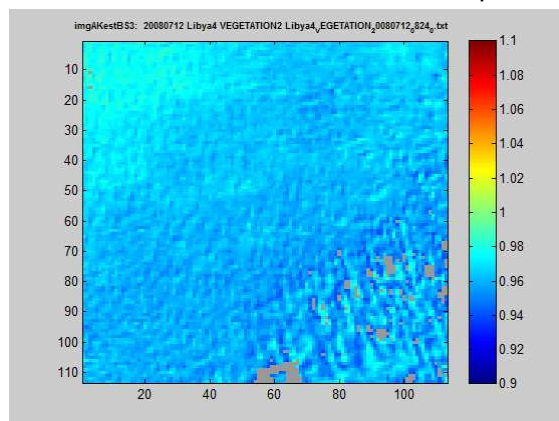


Figure 38: Map of reflectance ratio in the NIR band

The histograms of the reflectance ratio in the 4 bands are the following:

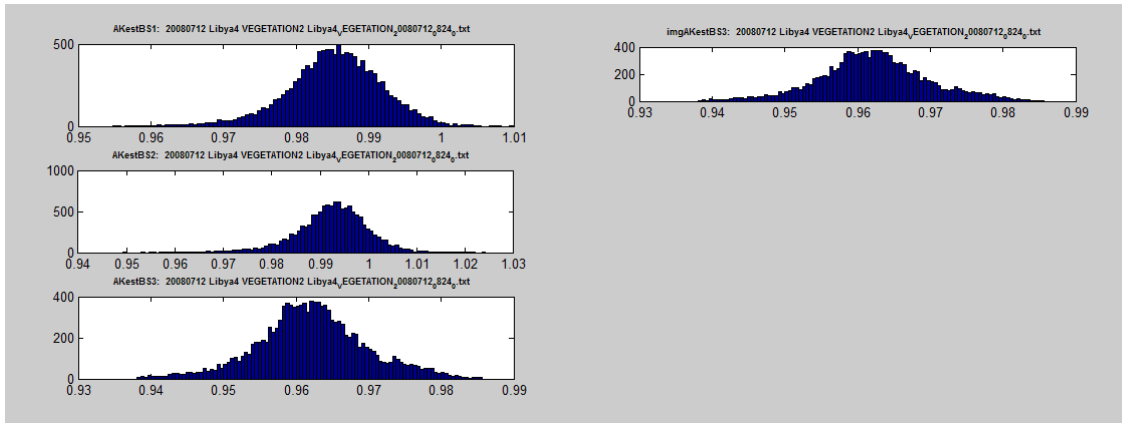


Figure 37: Ratio of Measured to Simulated TOA reflectance histograms

4.5.2 Multiyear results

The change in sensor radiometry is estimated by computing the mean of the measured to simulated TOA reflectances ratio for all available acquisitions. It is represented for the 4 bands in the figures below from 2008 to 2011.

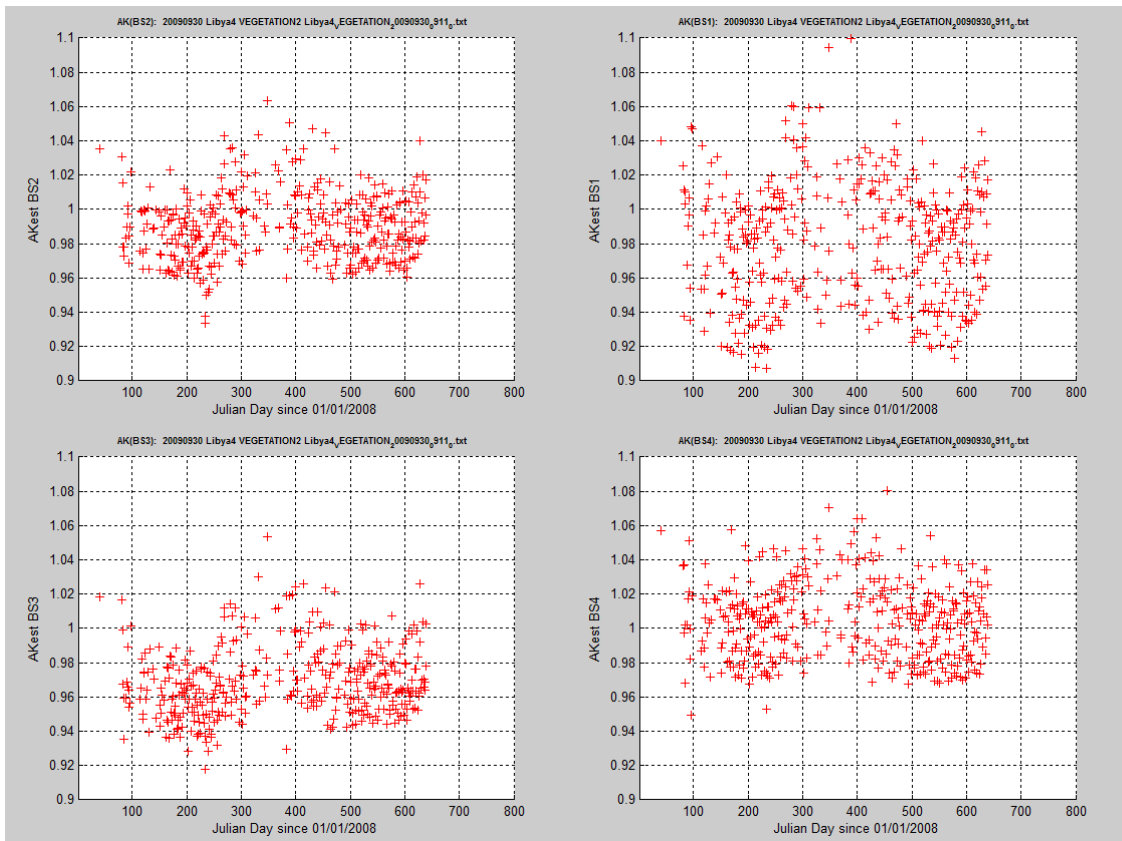


Figure 39: Temporal variability of the mean ratio between 2008 and 2011

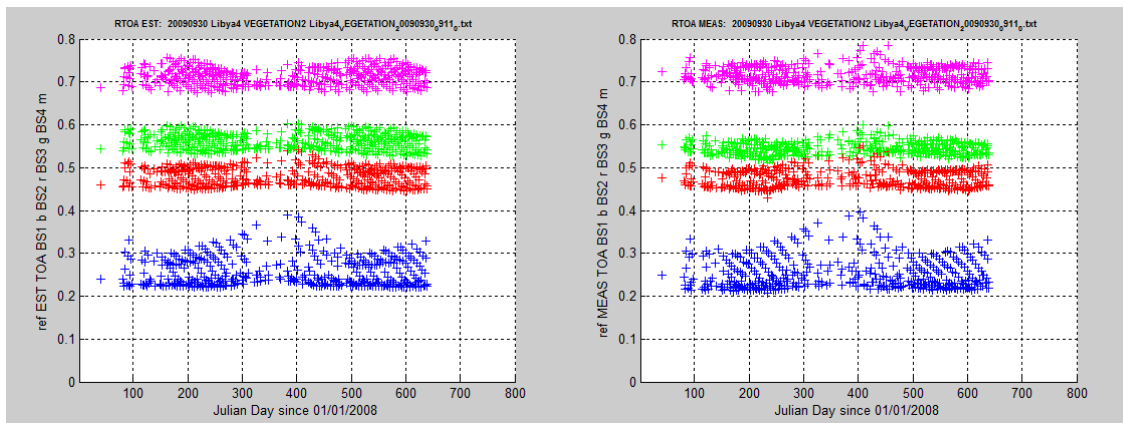


Figure 40: Temporal variability of the TOA reflectance (measured and simulated)

The variability of the ratio for four VEGETATION channels is plotted versus the mean solar zenith angle observed at the acquisition date.

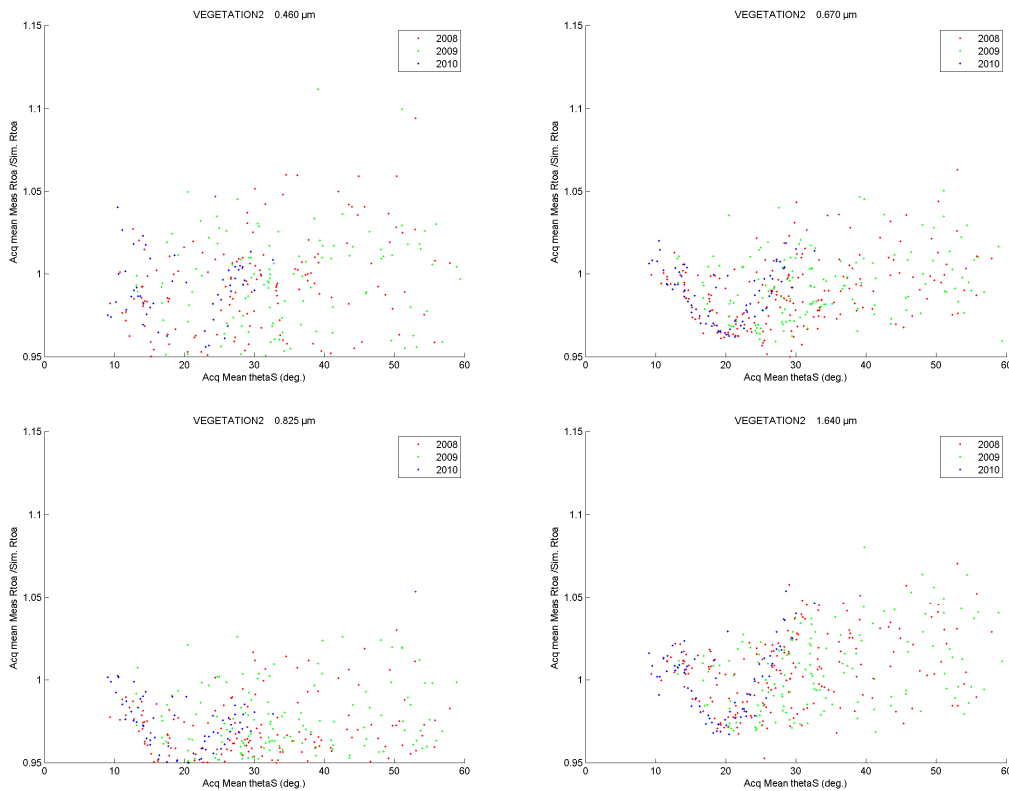


Figure 27: Temporal variability of the mean ratio of Measured to Simulated TOA reflectance versus Solar zenith Angle

5 Error Analysis

The following list recaps the main post of uncertainties.

The uncertainties in the method include:

- Uncertainties in the radiative computation: If the solar zenith angle is smaller than 75°, the accuracy of the radiative transfer calculation based on plane parallel approximation is better than 10^{-3} in reflectance units (Vermote and Tanré, 1992).
- BRDF modelling errors: Error on MODIS BRDF modelling are transferred to the others sensors.
- Spectral interpolation : Assess the spline function and how extrapolation are managed (for instance MERIS 412 nm)
- Spectral band knowledge used for spectral interpolation
- Geophysical uncertainties:
 - ✦ Gaseous absorption:
 - ✦ ozone amount : 5%
 - ✦ water vapour amount: 20%
 - ✦ Rayleigh optical thickness: 1.5 % resulting from an error of 15 hPa on pressure.
 - ✦ aerosol type: low, 1.5%
 - ✦ Aerosol AOT : no temporal variations
 - ✦ SMAC method

- End of the document -